

← Formatted: Header

Style Definition: Header: Font: (Asian) SimSun

1 Ensembling Differentiable Process-based and Data-driven Models with

2 Diverse Meteorological Forcing Datasets to Advance Streamflow Simulation

3 Peijun Li¹, Yalan Song¹, Ming Pan², Kathryn Lawson¹, Chaopeng Shen¹

4 ¹Civil and Environmental Engineering, The Pennsylvania State University, University Park,
5 PA, USA

6 ²Center for Western Weather and Water Extremes, Scripps Institution of Oceanography,
7 University of California San Diego, La Jolla, CA, USA

8 *Correspondence to: Peijun Li, pqj5336@psu.edu; Chaopeng Shen, cshen@engr.psu.edu

9 ← Formatted: Normal, Line spacing: single

10 Formatted: Font color: Auto

Abstract

11 Streamflow simulations viaproduced by different hydrological models havedifferent
12 featuresexhibitdistinctcharacteristics and can provide valuable information afterbeingwhen
13 ensembled. WhileHowever, few studies have focused on ensembling simulations viafrom
14 models with significant structural differences and evaluating them under both temporal and
15 spatial tests. Here we systematically evaluated and utilized the simulations from two highly
16 different models with great performances: a purely data-driven long short-term memory
17 (LSTM) network and a physics-informed machine learning (“differentiable”) HBV
18 (Hydrologiska Byråns VattenavdelningVattenbalansavdelning) model (δ HBV). To effectively
19 display the features of the two models, multiple forcing datasets are employedandutilizedin
20 twoways. The results show that the simulations of LSTM and δ HBV have distinct features
21 and complement each other well, leading to better Nash-Sutcliffe model efficiency coefficients
22 (NSE) and improved high-flow and low-flow metrics across all spatiotemporal tests, compared
23 to within-class ensembles. Ensembling models trained on a single forcing outperformed a
24 single model using fused forcings, challenging the paradigm of feeding all available data into
25 a single data-driven model. Most notably, δ HBV significantly enhanced spatial interpolation

26 when incorporated into LSTM, and provided even more prominent benefits for spatial
27 extrapolation where the LSTM-only ensembles degraded significantly, attesting to the value of
28 the structural constraints in δ HBV. These advances set new benchmark records on the well-
29 known CAMELS (Catchment Attributes and Meteorology for Large-sample Studies)
30 hydrological dataset, reaching median NSE values of ~ 0.83 for the temporal test (densely
31 trained scenario), ~ 0.79 for the ungauged basin test (PUB, Prediction in Ungauged Basins),
32 and ~ 0.70 for the ungauged region test (PUR, Prediction in Ungauged Regions). This study
33 advances our understanding of how various model types, each with distinct mechanisms, can
34 be effectively leveraged alongside multi-source datasets across diverse scenarios.

35

36 **Highlights**

- 37 • Combining LSTM and δ HBV with diverse forcings sets new accuracy benchmarks
- 38 • Ensembling models with one forcing outperforms merging forcings as an input
- 39 • δ HBV and LSTM together always increase NSEs, especially spatial generalization
- 40 • δ HBV provides valuable spatial constraints in the deterministic ensemble simulations
- 41 • δ HBV and LSTM have different error characteristics that can be offset in an ensemble

42

43 **Keywords**

44 Streamflow simulation, differentiable model, deep learning, hybrid modeling, multi-source
45 fusion

46

47 **1. Introduction**

48 Streamflow, a critical component of the global hydrophere, profoundly influences both
49 human society and natural ecosystems (Lins and Slack, 1999). Accurate simulation and
50 prediction of streamflow yield numerous benefits, including improved flood prevention
51 strategies (Brunner et al., 2021). Hydrological models serve as indispensable tools for
52 achieving this objective and can be traditionally categorized into two types: data-driven models
53 ([Feng et al., 2020](#); [Kratzert et al., 2018](#); [Liu et al., 2024](#); [Nearing et al., 2024](#)) ([Feng et al., 2020](#);
54 [Kratzert et al., 2018](#); [Liu et al., 2024](#); [Nearing et al., 2024](#)) and process-based (or physically-
55 based) models (Newman et al., 2017; Paul et al., 2021). Data-driven models, exemplified by
56 long short-term memory (LSTM) ([Feng et al., 2020](#); [Kratzert et al., 2018](#)) and transformer ([Liu](#)
57 et al., 2024) networks, excel in learning patterns from multi-source data ([Li et al., 2023b, 2024](#);
58 [Liu et al., 2022](#); [Nearing et al., 2024](#)) ([Li et al., 2023b, 2024](#); [Liu et al., 2022](#); [Nearing et al.,
59 2024](#)) and generally achieve high performance. However, they often lack interpretability and

← Formatted: Header

← Formatted: Font color: Auto

← Formatted: Outline numbered + Level: 1 + Numbering Style: Bullet + Aligned at: 0" + Indent at: 0.29"

← Formatted: Font color: Auto

← Formatted: Font color: Auto

60 may not resolve extreme values very well (Li et al., 2020a; Song et al., 2025). (Li et al., 2020a;
61 Song et al., 2025b). Conversely, process-based models, derived deductively from physical laws
62 or conceptualized views of natural systems, offer insights into internal hydrological processes
63 but may exhibit weaker performance due to structural inadequacies (Li et al., 2020a; Zhang et
64 al., 2019).

65 To combine the benefits and counteract the weaknesses of these two kinds of models,
66 many efforts have been made to incorporate physical constraints and structures into data-driven
67 models to align with fundamental physical principles, such as mass and water balances (Bandai
68 and Ghezzehei, 2021; Wang et al., 2020; Xie et al., 2021). The most seamless integration uses
69 neural networks to provide parameterizations or missing process representations for process-
70 based models (Aboelyazeed et al., 2023; Bindas et al., 2024; Feng et al., 2022; Jiang et al.,
71 2020; Kraft et al., 2022; Rahmani et al., 2023; Song et al., 2024b; Tsai et al., 2021). These
72 differentiable models (Shen et al., 2023) connect (flexible amounts of) prior physical
73 knowledge to neural networks, and have displayed many advantages, including improved
74 computational efficiency and prediction of untrained variables (Tsai et al., 2021), spatial
75 generalization (Feng et al., 2023b), and representation of extremes (Song et al., 2025). (Song et
76 al., 2025b). However, it is also unclear whether current differentiable models, e.g., δHBV, the
77 Hydrologiska Byråns Vattenbalansavdelning (HBV) model implemented within a
78 differentiable framework (Feng et al., 2023b; Shen et al., 2023; Song et al., 2025) (Feng et al.,
79 2023b; Shen et al., 2023; Song et al., 2025b), have unique bias characteristics that are
80 associated with the process-based parts of their structures that cannot be reduced once the
81 equations are prescribed.

82 Orthogonal to such efforts are ensemble simulations (Yu et al., 2024), which combine
83 many members with different biases and uncertainties to mitigate their respective biases in
84 deterministic predictions. Many previous studies have tried ensemble methods to improve

85 streamflow (Clark et al., 2016; Zounemat-Kermani et al., 2021) based on many factors, like
86 initial conditions (e.g., initial weights and biases in LSTM (Kratzert et al., 2018)), data used
87 for parameterization (Feng et al., 2021), and objective functions (Lin et al., 2024). These
88 studies generally use one model to generate the differences among the ensemble members.
89 Furthermore, some studies (Dion et al., 2021; Solanki et al., 2025) have utilized simulations
90 from multiple different models but are limited to process-based models ~~and resulted, resulting~~
91 in ensemble simulations that are better than each individual member. Thus far, however, most
92 studies ~~focus~~ have focused on ~~the~~ simulations from only similar models or model types, and
93 little work has tested an ensemble across the boundary of model types, ~~especially particularly~~
94 between data-driven, process-based, and hybrid models, especially on a large number of
95 samples. Presumably, if each model has its own unique bias, data-driven and process-based
96 models are likely to exhibit greater differences due to their inherently distinct characteristics.
97 It remains unclear whether ensembling across model types should bring benefits to
98 deterministic predictions. Furthermore, grounded in the process-based model, the differentiable
99 process-based hydrological model, such as δHBV, significantly enhances performance
100 compared to traditional process-based models, while on the other hand introducing greater
101 uncertainty regarding its potential benefits when ensembled. Moreover, previous studies have
102 primarily focused on evaluating ensemble simulations for temporal predictions. However,
103 streamflow simulation under spatial extrapolation scenarios presents greater challenges, and
104 findings from temporal tests may not be directly applicable in this context.

105 It is known that the performance of any type of hydrologic model heavily depends on the
106 quality of input data, particularly meteorological forcing data (Bell and Moore, 2000; Yao et
107 al., 2020), and other inputs, like the uncertainties of initial conditions, can be mitigated via
108 warming up (Yu et al., 2019). While independent forcing datasets excel in certain aspects, they
109 each carry different error characteristics (Beck et al., 2017; Behnke et al., 2016; Newman et al.,

← Formatted: Header

110 2019) and accordingly affect the hydrological models in different ways. In order to fully display
111 the different features between LSTM and δ HBV, multiple forcing datasets could be considered.
112 Given the utilization of multiple forcing datasets, one could choose to use data fusion to
113 combine them into a single coherent model input (Kratzert et al., 2021; Sawadekar et al., 2025),
114 or to pass each forcing dataset through a model and then afterwards combine the multiple
115 outputs in an ensemble. It is not clear which approach is more beneficial.

116 Considering the knowledge gaps discussed above, we sought to answer several research
117 questions:

- 118 1. Will a cross-model-type ensemble of LSTM and δ HBV improve deterministic
119 streamflow prediction more than a within-class ensemble?
- 120 2. Is it better to use multiple forcings in one model or to ensemble multiple models, each
121 with a different forcing input?
- 122 3. Do process-based equations bring unique value to an ensemble, especially in terms of
123 spatial generalizability?

← Formatted: Outline numbered + Level: 1 + Numbering Style:
1, 2, 3, ... + Start at: 1 + Alignment: Left + Aligned at: 0.25"
+ Indent at: 0.5"

124 The remainder of this paper is structured as follows: Sect. 2 outlines the hydrological data
125 and models used in this study, as well as the experimental design. Results and discussions are
126 presented in Sect. 3, with conclusions provided in Sect. 4.

127

128 **2. MaterialMaterials and Methodsmethods**

129 2.1. The CAMELS hydrologic dataset

Formatted: Font color: Auto

Formatted: Font color: Auto

Formatted: Font color: Auto

130 The Catchment Attributes and Meteorology for Large-sample Studies (CAMELS) dataset
131 (Addor et al., 2017) is widely employed for hydrological model evaluation and community
132 benchmarking. The CAMELS dataset encompasses 671 basins distributed across the
133 conterminous United States, with basin sizes ranging from 1 to 25,800 km² (median: 335 km²).
134 This standardized and publicly available dataset serves as a benchmark for evaluating various

← Formatted: Header

135 hydrological models, with LSTM models trained on this dataset often serving as a reference
136 point for comparing other models (Kratzert et al., 2021). CAMELS provides basin-scale data,
137 including streamflow observations and static basin attributes, as well as forcing datasets from
138 three independent sources: Daymet (Thornton et al., 1997), North American Land Data
139 Assimilation System (NLDAS) (Xia et al., 2012), and Maurer (Maurer et al., 2002). Each of
140 the three meteorological forcing datasets operates at a daily temporal resolution, encompassing
141 precipitation, temperature, vapor pressure, and surface radiation variables, with daily
142 temperature extrema of NLDAS and Maurer supplemented from Kratzert et al. (2021). These
143 three meteorological forcing datasets have methodological distinctions in spatial resolution,
144 data generation approaches, and temporal processing (Behnke et al., 2016; Kratzert et al., 2021).
145 Exemplary plots illustrating the differences among the three meteorological forcing datasets
146 are provided in Appendix B. These features can lead to dataset-specific error characteristics
147 and make them valuable for displaying the distinct features of different model types. All model
148 inputs used in this study are detailed in Table C1.

← Formatted: Line spacing: Double

149
150 2.2. Long short-term memory

151 As one kind of deep learning algorithm, long short-term memory (LSTM) (Hochreiter and
152 Schmidhuber, 1997) has unique structures like hidden states and gates activated by the tanh
153 and sigmoid functions (Li et al., 2023a), respectively. These features enable LSTM to excel in
154 streamflow simulation tasks ([Feng et al., 2020](#); [Kratzert et al., 2018](#); [Nearing et al., 2024](#)) ([Feng](#)
155 [et al., 2020](#); [Kratzert et al., 2018](#); [Nearing et al., 2024](#)). In the current benchmark framework,
156 LSTM models are trained using dynamic atmospheric forcings and static basin attributes as
157 inputs, with streamflow as the target output, making it perform well in both temporal and spatial
158 tests (Figure 1a). In this work, for cross-group comparability, we used the LSTM model and
159 its hyperparameters as reported in Kratzert et al. (2021).

160

161 2.3. Differentiable HBV model (δ HBV)

162 The Hydrologiska Byråns Vattenbalansavdelning (HBV) model is a parsimonious bucket-
163 type hydrologic model that simulates various hydrological variables, including snow water
164 equivalent, soil water, groundwater storage, evapotranspiration, quick flow, baseflow, and total
165 streamflow (Aghakouchak and Habib, 2010; Beck et al., 2020; Bergström, 1976, 1992).
166 Recently demonstrated differentiable HBV (δ HBV) model (Feng et al., 2023b; Shen et al.,
167 2023; Song et al., 2024b) incorporates deep neural networks for both regionalized
168 parameterization and missing process representations within a differentiable programming
169 framework that supports “end-to-end” training (Figure 1b). This innovation enables δ HBV to
170 effectively learn from data while obeying physical laws, resulting in high-level performance
171 for streamflow simulations. From the perspective of process-based modeling, LSTM is a
172 regionalized parameter provider that leverages the autocorrelated nature of its inputs to impose
173 an implicit spatial constraint on the generated parameters.

174 ~~In this study, we used δ HBV1.1p (Song et al., 2024b, 2025) which is an updated version~~
175 ~~from δ HBV1.0. In this study, we used δ HBV1.1p (Song et al., 2024b, 2025b), which is an~~
176 ~~updated version of δ HBV1.0 (Feng et al., 2022, 2023b). The main improvement is the addition~~
177 ~~of a capillary rise module, which enhances the characterization of low flows. Other~~
178 ~~modifications include the use of three dynamic parameters during the warm-up, training, and~~
179 ~~test periods, the removal of log-transform normalization for precipitation, and the adoption of~~
180 ~~NSE as the loss function for model training. The basic equations in δ HBV are as follows:~~

181 ~~. The main improvement is the addition of a capillary rise module, which enhances the~~
182 ~~characterization of low flows. Other modifications include three modifications to address high-~~
183 ~~flow simulation challenges: the use of three dynamic parameters (γ, β, k_0) (Song et al., 2025b);~~
184 ~~the removal of log-transform normalization for precipitation; and the adoption of the~~

185 normalized squared-error loss function (Frame et al., 2022; Kratzert et al., 2021; Song et al.,
186 2025a, b; Wilbrand et al., 2023). We also maintain dynamic parameters during warm-up
187 periods. Although this provides only marginal benefits and increases computational costs, it
188 yields a more realistic representation and reduces uncertainties associated with initial
189 conditions. The basic equations in δ HBV are as follows:

$$\theta = LSTM_w(\bar{x}, \overline{A_{attr}}) \quad (1)$$

$$Q = HBV(x, \theta) \quad (2)$$

$$W_{opt} = argmin_w(L(Q, Q^*)) \quad (3)$$

190 where θ are the dynamic or static physical parameters, w denotes the weights and biases of
191 LSTM, x includes the basin-averaged meteorological forcings, such as precipitation, mean
192 temperature, and potential evapotranspiration, with \bar{x} representing their normalized versions.

193 Similarly, $\overline{A_{attr}}$ consists of normalized observable basin-averaged attributes, encompassing
194 basin area, topography, climate, soil texture, land cover, and geology (Table C1). Precipitation
195 and mean temperature are from CAMELS, while potential evapotranspiration is calculated
196 based on the Hargreaves (1994) method using mean, maximum, and minimum temperatures
197 along with basin latitudes, all from data described in sect. 2.1. Q and Q^* are the streamflow
198 simulations (model outputs) and observations (as provided in CAMELS), respectively. HBV
199 is implemented on PyTorch so it is programmatically differentiable: all steps store information
200 related to gradient calculations during backpropagation, allowing this model to be trained
201 together with neural networks in an end-to-end fashion. More details about differentiable HBV
202 can be found in previous studies (Feng et al., 2022; Song et al., 2024b). The details of some
203 particularly relevant HBV processes are described in Appendix A.

204

205 2.4. Experimental Design

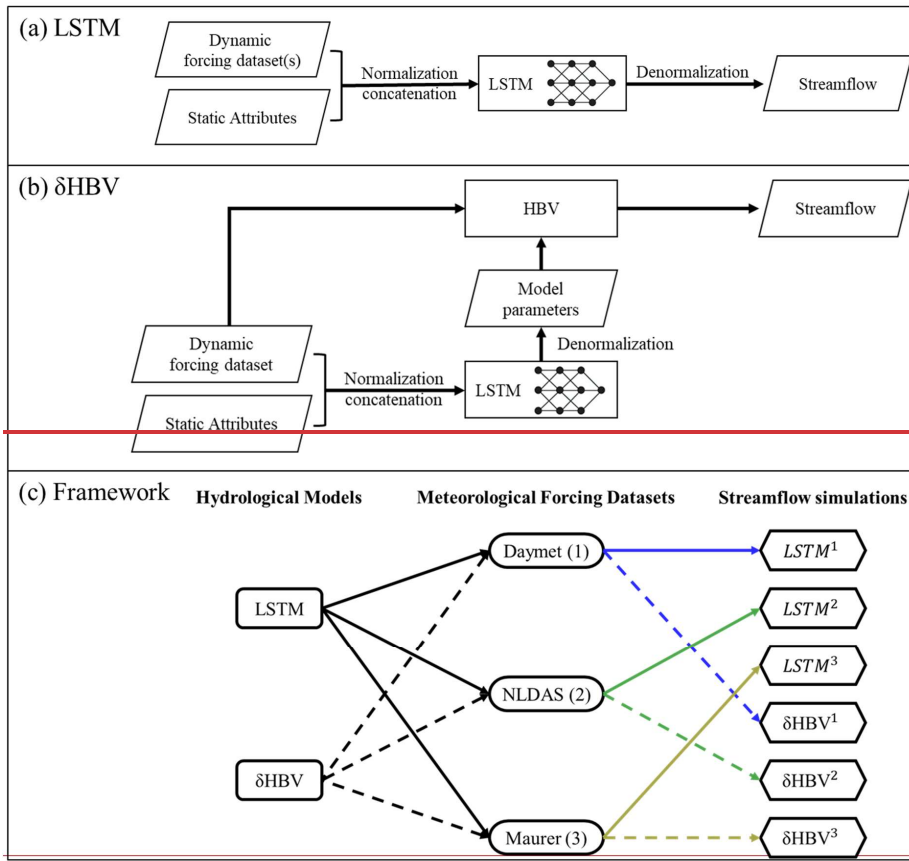
← Formatted: Header

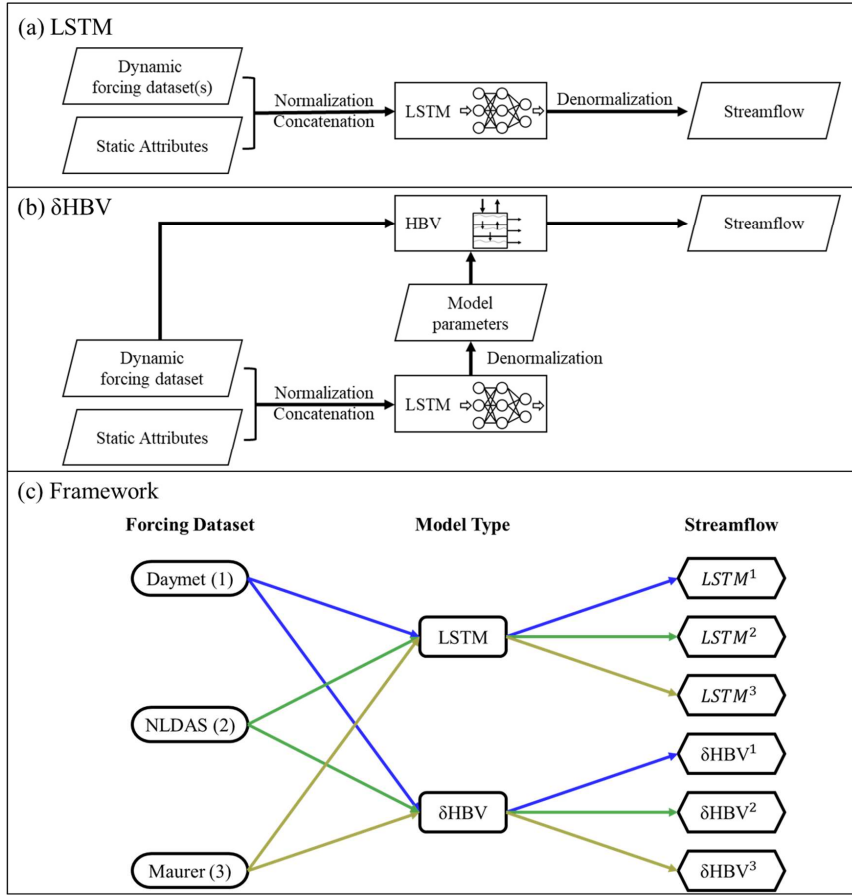
← Formatted Table

← Formatted: Highlight

206 In this study, we trained the two models ~~in highly of very~~ different types (LSTM and δ HBV)
207 ~~using), each with one of~~ three meteorological forcing datasets (Daymet, NLDAS, and Maurer),
208 resulting in six corresponding streamflow simulations (Figure 1c) for each different test
209 scenario (see sect. 2.5 for additional information). The training processes of LSTM and δ HBV
210 followed Kratzert et al. (2021) and Feng et al. (2023b), respectively. Test results and
211 performance metrics for all models are reported for the 531-basin subset that excludes those
212 with areas larger than 2,000 km² or with more than a 10% discrepancy between different basin
213 area calculation methods (Newman et al., 2017).

214 To generate ensembles, we tested various weighting strategies and ultimately employed
215 averaging to combine the six single-forcing, single-model-type simulations, as it yielded the
216 best performance. To better describe various combinations including cross-model ensembles,
217 these simulations were categorized into six groups (Table 1). A shorthand notation is used
218 throughout the remainder of this work to describe the forcing datasets and ensembles. Daymet,
219 NLDAS, and Maurer are abbreviated as superscripts 1, 2, and 3, respectively. The + symbol is
220 used to group model types being ensembled, while superscript clustering (e.g., ¹² or ¹²³) is used
221 to group the meteorological forcing types being ensembled, with parentheses indicating that
222 the superscripts apply to all model types within. For example, $(LSTM + \delta HBV)^{123}$ could be
223 explicitly written as $LSTM^1 + LSTM^2 + LSTM^3 + \delta HBV^1 + \delta HBV^2 + \delta HBV^3$. To compare
224 two different strategies to utilize the multiple meteorological forcing datasets and to benchmark
225 against the previously highest performance, we additionally trained a single LSTM model using
226 all three forcing datasets as simultaneous inputs as done by Kratzert et al. (2021), ~~referred to~~
227 as LSTM^{multi} (the last row in Table 1).





230

231 *Figure 1. (a) The LSTM structure, (b) the δHBV structure, and (c) the framework to generate*
 232 *the six individual ensemble members of the streamflow simulations, in which different colors*
 233 *of arrow lines denote the different meteorological forcing datasets (also denoted as 1, 2, 3, and the arrow line styles (solid and dashed lines) indicate the LSTM and δHBV models, respectively.*

236 *Table 1. (a) The six groups of streamflow simulations, and (b) the streamflow simulation via*
 237 *LSTM based on a different strategy to utilize, in which three meteorological forcing datasets*
 238 *were combined as a single set of inputs* (Kratzert et al., 2021). Superscripts 1, 2, and 3 denote
 239 *Daymet, NLDAS, and Maurer, respectively. The ensemble across forcings (“ef”) superscript*
 240 *indicates an ensemble of model simulations, each of which uses a different single*
 241 *meteorological forcing, e.g., $LSTM^{12}$ means the average of $LSTM^1$ and $LSTM^2$.*

242

243

(a) Six Groups of Streamflow Simulations		
Group Name	Group Members	
LSTM	LSTM ¹ , LSTM ² , LSTM ³	
δHBV	δHBV ¹ , δHBV ² , δHBV ³	
LSTM+δHBV	(LSTM+δHBV) ¹ , (LSTM+δHBV) ² , (LSTM+δHBV) ³	
LSTM ^{ef}	LSTM ¹² , LSTM ¹³ , LSTM ²³ , LSTM ¹²³	
δHBV ^{ef}	δHBV ¹² , δHBV ¹³ , δHBV ²³ , δHBV ¹²³ ,	
(LSTM+δHBV) ^{ef}	(LSTM+δHBV) ¹² , (LSTM+δHBV) ¹³ , (LSTM+δHBV) ²³ , (LSTM+δHBV) ¹²³	
(b) Using forcing datasets as simultaneous inputs to an LSTM		
Streamflow Simulation	Model Type	Meteorological Forcing Dataset
LSTM ^{multi}	LSTM	Daymet, NLDAS, Maurer

← Formatted: Header

← Formatted Table

244 2.5. Evaluation Scenarios and Criteria

245 The above cases were comprehensively evaluated for performance in temporal
246 extrapolation (Feng et al., 2022; Kratzert et al., 2018), as well as two types of spatial
247 generalization: prediction in ungauged basins (PUB) (Feng et al., 2023b; Kratzert et al., 2019),
248 and prediction in ungauged regions (PUR) (Feng et al., 2021, 2023b):

249

- **Temporal Test:** Models were trained using data from all basins and tested across different periods.

250

- **PUB Test:** Models were trained on randomly selected subsets from all basins and tested on the remaining basins during the same time period.

251

- **PUR Test:** Different from the PUB test, basins were grouped into continuous regions, one of which was selected to comprise the group of testing basins while the others were used for training.

252

253

254 Temporal generalization is generally considered to be the easiest of these tests. In terms
255 of spatial generalization, which approximates data-sparse scenarios, the PUB test is an example
256 of spatial interpolation, whereas the PUR test involves spatial extrapolation. The PUR test is
257 widely regarded as the most challenging and may therefore produce findings that differ
258 significantly from those in other scenarios. In this study, all basins were divided into 10
259 spatially stratified groups for the PUB test and 7 fully disjoint regional groups for the PUR test
260 (Table 2) in the same way as Feng et al. (2023b). The spatial extent of the 7 regions for the
261 PUR test is also shown in Figure 3(c1-c2).⁻ Therefore, we conducted 10 rounds for the PUB
262 test and 7 rounds for the PUR test, with a different group held out for testing in each round.
263 Model performance was evaluated after concatenating the test results for all basins.
264

267 *Table 2. Differences of temporal, PUB, and PUR tests.*

Test Scenario	Training		Testing	
	Basin	Time	Basin	Time
Temporal	All ^a	1980-1995 ^b	All	1995-2010
PUB	Random nine-tenths	1980-1999	Holdout ^c	1995-1999
PUR	Random six of seven regions	1980-1999	Holdout	1995-1999

268 ^a δ HBV training followed Feng *et al.* (2023b) using all 671 CAMELS basins, while LSTM
 269 training followed Kratzert *et al* (2021) using the selected 531-basin subset. Test results and
 270 performance metrics for all models are reported for the 531 basins.

271 ^bEach hydrological year spans from October 1st to September 30th of the following year.

272 ^cIn the PUB and PUR tests, models are run for 10 and 7 rounds, respectively, with the group
 273 held out for testing changed in each round. The simulation performance was evaluated after
 274 concatenating the test results for all basins.

275

276 We repeated all the simulations with three different random seeds. Therefore, all the
 277 simulations come from a total of $(2 \times 3 + 1) \times (1 + 10 + 7) \times 3$ trained models. The first factor
 278 represents the models: two model types (LSTM and δ HBV) trained separately with each of the
 279 three forcing datasets, along with $LSTM^{multi}$, a single model instance trained using all three
 280 forcing datasets simultaneously. The second factor accounts for the three types of tests
 281 (temporal, PUB, and PUR tests), and the last for the three random seeds. With respect to
 282 random seeds, we present two variations in the results, which are visually depicted in Figure
 283 C1. The results without “seed” as a subscript represent the average metric values from multiple
 284 streamflow simulations, each generated from a single model implementation, along with the
 285 corresponding uncertainties, visualized using error bars. The results marked with “seed” as a
 286 subscript are based on the average of multiple streamflow simulations conducted with different
 287 random seeds. In terms of computational cost, training LSTM (30 epochs) and δ HBV (50
 288 epochs) for temporal testing under a single meteorological forcing dataset takes approximately

← Formatted: Header

← Formatted Table

← Formatted: Header

289 5 and 21 hours, respectively, using a single NVIDIA Tesla V100 GPU.

290 We calculated several well-established performance metrics: Nash-Sutcliffe model
291 efficiency coefficient (*NSE*) (Nash and Sutcliffe, 1970), Kling-Gupta model efficiency
292 coefficient (*KGE*) (Kling et al., 2012), percent bias (*PBIAS*), and root-mean-square error
293 (*RMSE*). We also considered *RMSE* values for high (top 2% “peak” flow, *highRMSE*), low
294 (bottom 30% “low” flow, *lowRMSE*), and mid-range (the remaining flow, *midRMSE*) flow
295 conditions (Yilmaz et al., 2008). These metrics were computed for each basin and aggregated
296 into error bars and cumulative density functions (CDFs). ~~Detailed descriptions of these metrics
297 and their calculations are available in Table C2. For brevity, the main text primarily reports
298 NSE values, and other metric values are provided in Appendixes D and E. For brevity, the main
299 text primarily reports NSE values, and other metric values are provided in Appendices D and
300 E. Furthermore, we use the spread values (Li et al., 2021; Reichle and Koster, 2003) to
301 investigate ensemble variability and explore model complementarity. Detailed descriptions of
302 these metrics and their calculations are available in Table C2.~~

303

304 **3. Results and Discussion**

305 3.1. Temporal extrapolation

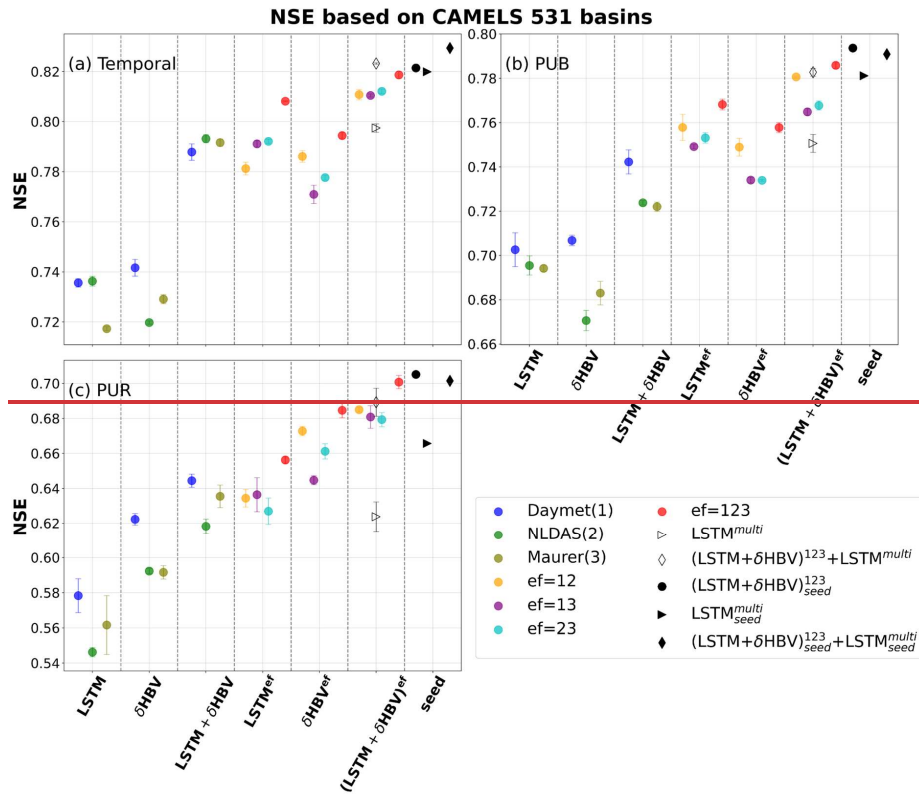
← Formatted: Font color: Auto

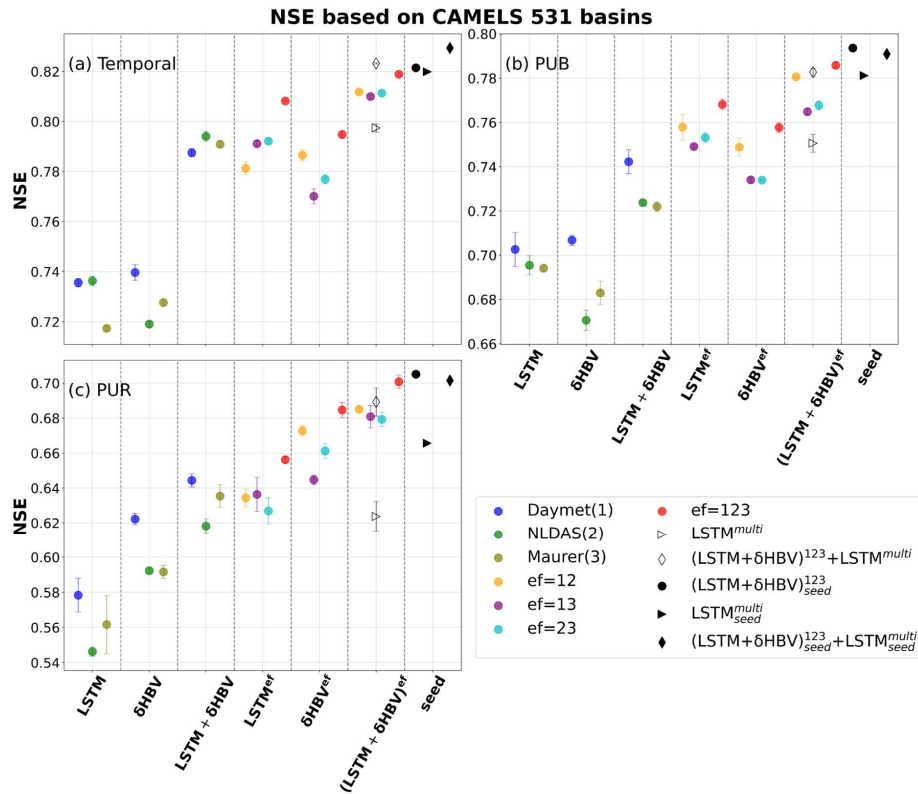
← Formatted: Font color: Auto

306 For the temporal test, in which models were trained and tested on the same basins but in
307 different time periods, we found that cross-model-type ensembles noticeably surpassed the
308 within-class ensembles when other conditions were the same, with small uncertainties ~~as~~
309 shown by the error bars in Figure 2. With a single forcing dataset, the median *NSE* was
310 elevated from ~0.735 for LSTM to ~0.79 with δ HBV added, though δ HBV performance was
311 similar to LSTM (~0.74 under Daymet). Even after LSTM achieved very high performance
312 when its simulations, each derived separately from different meteorological forcing datasets,
313 were ensembled ($ef = 123$, ~0.808), adding δ HBV still improved the results to ~0.818. This

314 finding was robust for all different combinations of the tested meteorological forcing datasets.
315 Conversely, adding LSTM also helped to improve δ HBV ensembles. These results highlight
316 the benefits of the cross-model-type ensemble framework, and indicate distinct simulation
317 features *via* [for](#) each model type. LSTM is a data-driven method that has low bias and large
318 variance. [Errors with data](#)[Data errors](#) (Li et al., 2020b), different sampling strategies (Nai et al.,
319 2024), or even different weight initializations (Narkhede et al., 2022) can lead to substantively
320 different outcomes. [On the other hand](#)[Conversely](#), δ HBV may have a smaller variance but a
321 larger bias due to the fixed HBV formulation (Moges et al., 2016) for some scenarios like low
322 flows (Feng et al., 2023b; Song et al., 2024b) or in basins with significant water uses [\(Song et](#)
323 [al., 2024a\)](#)[\(Song et al., 2024a\)](#). These errors with varying characteristics from different model
324 classes can partially offset each other in an ensemble. On a side note, δ HBV models seem more
325 reliant on the quality of the forcing data, as shown in Figure 2. δ HBV with the Maurer and
326 NLDAS forcing datasets generally performs worse than [it does](#) with Daymet [that, which](#) has
327 lower biases. However, even in those cases, the combination of LSTM and δ HBV was still
328 better than LSTM alone, attesting to the robustness of these benefits.

329
330

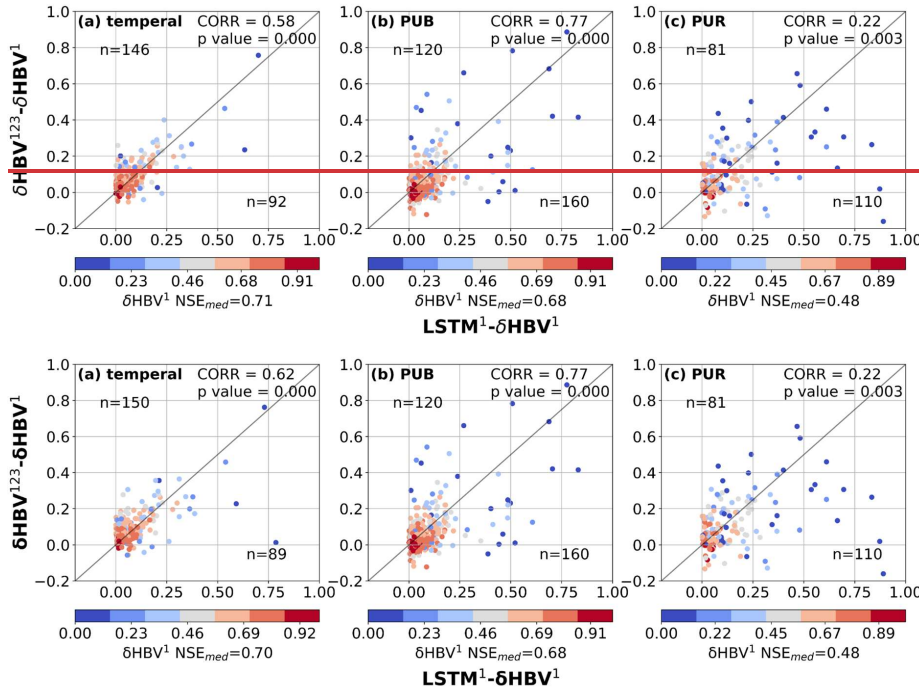




332

333 *Figure 2. Median NSE values for 531 CAMELS basins, indicating model and ensemble*
 334 *performances for (a) temporal, (b) prediction in ungauged basin (PUB), and (c) prediction in*
 335 *ungauged region (PUR) tests. Different simulations are represented by variously-shaped and*
 336 *-colored points, and are organized by ensemble group, listed along the x-axis: LSTM,*
 337 *δHBVδHBV, LSTM+δHBV, and their “ensemble forcing” counterparts, LSTM^{ef}, δHBV^{ef},*
 338 *and (LSTM + δHBV)^{ef}. LSTM^{multi} is a single LSTM model trained directly on all three*
 339 *forcing datasets at once. The superscript “ef” denotes the forcing datasets involved in each*
 340 *ensemble (choices of 1 for Daymet, 2 for NLDAS, and 3 for Maurer), while the “+” connects*
 341 *the model types used within an ensemble. The x-axis group and subscript “seed” indicate that*
 342 *simulation results were averaged based on three different random seeds (see Figure C1). Other*
 343 *points without “seed”, along with their corresponding error bars, are derived from the*
 344 *averages of metrics computed over repeated runs with three different random seeds. The error*
 345 *bar indicates one standard deviation above and below the average value for each simulation.*

346



347

348

349 *Figure 3. Scatter plots comparing the performance differences between hydrological models*
 350 *for the basins where LSTM outperformed δHBV (the basins where δHBV outperformed are not*
 351 *shown in this plot). The x-axis represents the NSE differences between LSTM¹ and δHBV¹*
 352 *(LSTM¹ - δHBV¹), while the y-axis shows the NSE differences between δHBV¹²³ and δHBV¹*
 353 *(δHBV¹²³ - δHBV¹). Points are color-coded according to the NSE values of δHBV¹. The*
 354 *correlation coefficient (CORR) and p values between the x-axis values and the y-axis values,*
 355 *along with the median NSE value of δHBV¹ (NSE_{med}) on these basins are also noted. We*
 356 *note that NSE is not additive and should in general generally not be subtracted. Here the*
 357 *purpose is only to confirm that basins where LSTM outperforms δHBV also tend to be those*
 358 *that benefit from the ensemble of forcings.*

359

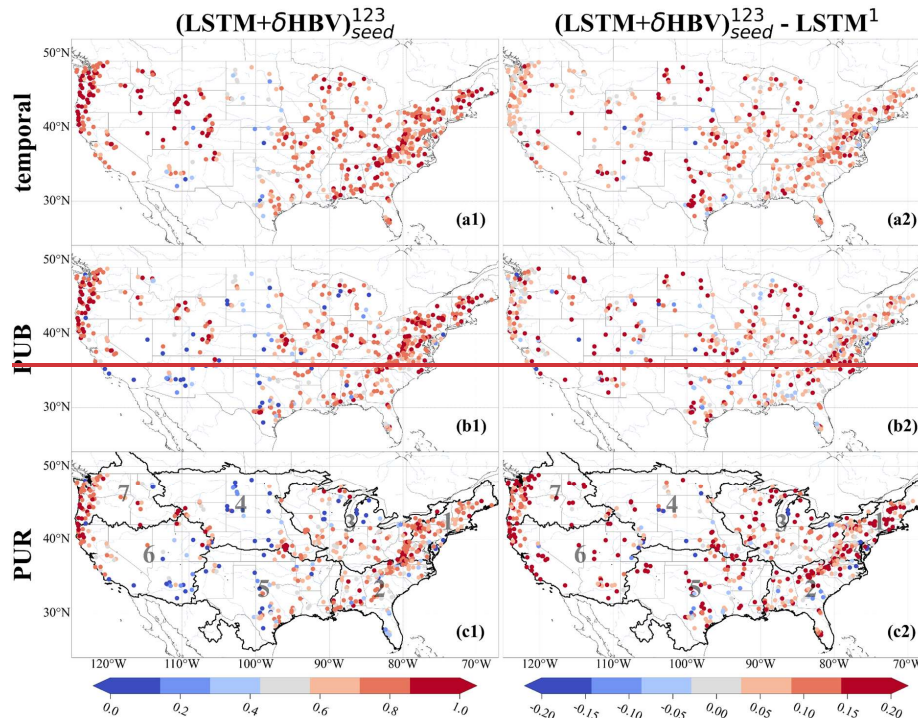
360 In the lower-performing basins where LSTM^1 had advantages over δHBV^1 , the ensemble
 361 of meteorological forcings δHBV^{123} also tended to be higher than δHBV^1 (Figure 3),
 362 suggesting that forcing quality was a significant reason behind the underperformance of δHBV^1
 363 in these basins. Similar patterns were also observed when analyzing $\text{RMSE}_{\delta\text{HBV}^2}$ and δHBV^3

364 values (Figure D1 [and Figure D2](#)). These basins previously contributed to LSTM's cumulative
365 distribution function of NSE diverging from that of δHBV^1 at the low end (Feng et al., 2022).
366 Forcing errors can exist in the form of systematic timing errors, low or high bias for larger
367 events, etc., which can be difficult for the mass-balanced conceptual HBV¹ structure to adapt
368 to these errors. Because the ensemble of forcings tends to suppress the errors in each forcing
369 source, part of the advantages of δHBV^{123} over δHBV^1 can be attributed to reducing forcing
370 bias or timing errors. Since the advantages of LSTM¹ over δHBV^1 also tend to occur with these
371 same basins, this also explains how LSTM¹ surpasses δHBV^1 in some basins with poorer-
372 quality forcings. In contrast to δHBV , LSTM has the innate ability to shift information in time
373 and moderately adjust the input scale. Moving from temporal validation to PUB to PUR
374 scenarios, the advantages of diverse forcing datasets appear to diminish, as evidenced by the
375 decreasing ratio of points above versus below the diagonal line, since the forcing error patterns
376 remembered by LSTM may not generalize well in space (discussed in more detail in sect. 3.2).
377

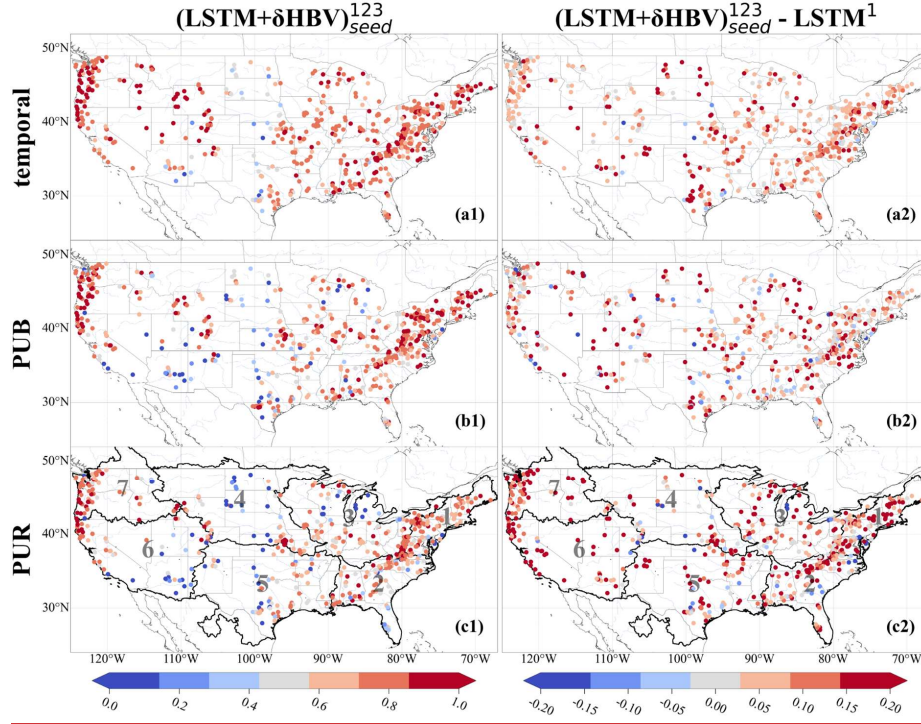
378 Ensembling streamflow simulations from different meteorological forcing datasets
379 demonstrates certain advantages over the previous approach of simultaneously sending
380 multiple forcings into [an MLa data-driven](#) model like LSTM (Kratzert et al., 2021).
381 Ensembling LSTM simulations each using a single forcing dataset ($LSTM^{123}$) resulted in an
382 NSE value of 0.8082, higher than that of 0.7974 from feeding multiple forcing datasets into a
383 single LSTM ($LSTM^{multi}$). This difference was more pronounced in the cross-model-type
384 ensemble, after including δHBV , compared to the previous within-class ensemble, and
385 particularly notable for the spatial generalization tests (to be discussed in more detail in Sect.
386 3.2), with specific metric values provided in Tables D1-D5. These results indicate that the
387 trained LSTM in $LSTM^{multi}$ may be overfitted to the significant redundant information in
388 these three forcing datasets, and that only LSTM cannot fully exploit the information hidden

389 in the multiple forcing datasets. Training separate ensemble members via different nonlinear
 390 hydrological processes, on the other hand, seems to allow different bias features to emerge with
 391 separate forcing datasets, accordingly mitigating them during the subsequent ensembling
 392 process.

393



394



395 *Figure 4. Spatial distributions of NSE values over 531 basins. Subplots are arranged in rows, indicating (a) temporal, (b) PUB, and (c) PUR test results, and columns, denoting (1) NSE values from $(LSTM + \delta HBV)_{seed}^{123}$ and (2) the differences between these NSE values and those of $LSTM^1$ (models using only forcing 1, Daymet). For $LSTM^1$, each NSE value reported was the average of three NSE values from three simulations using three different random seeds. The seven continuous regions used to divide up basins for the PUR test are outlined and numbered in the PUR test maps.*

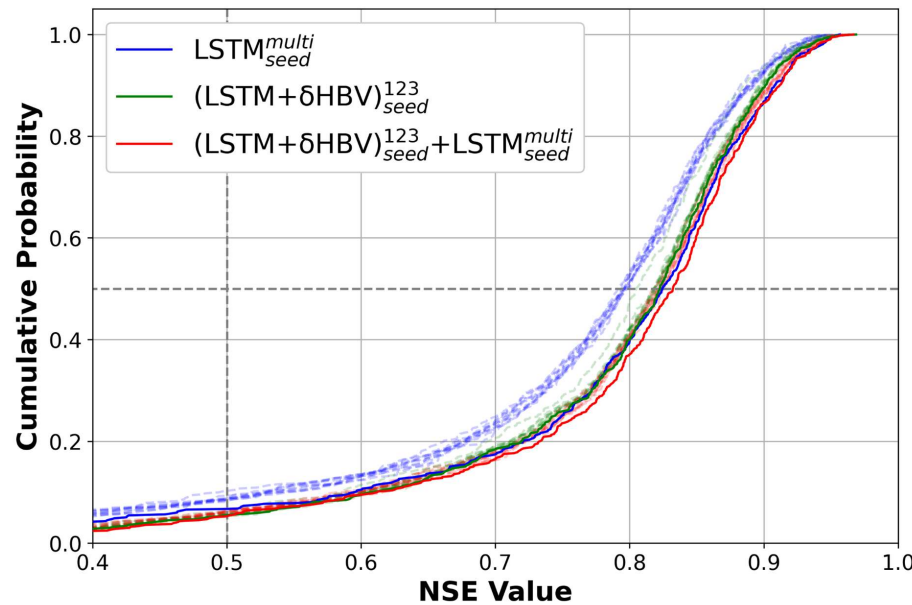
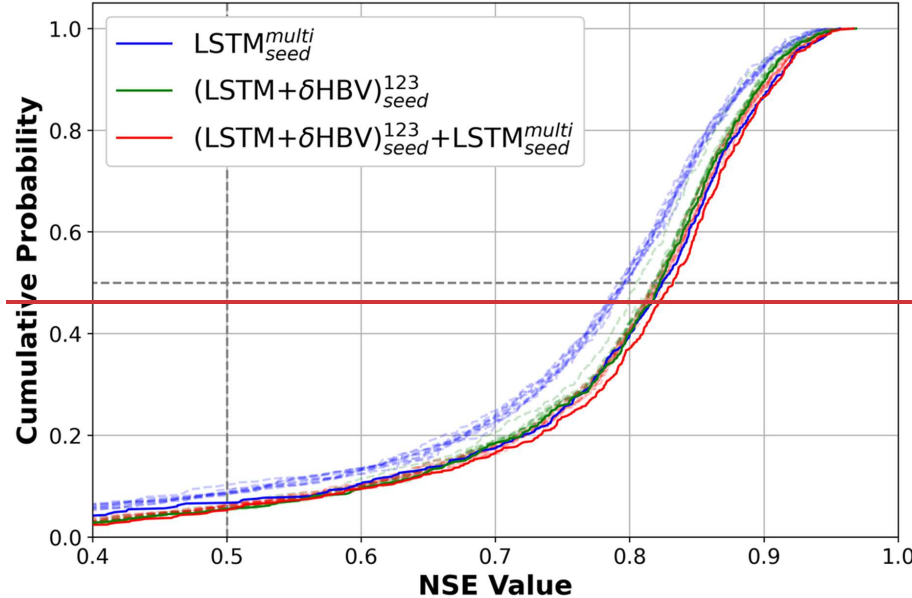
403

404 Our most diverse ensemble, $(LSTM + \delta HBV)_{seed}^{123} + LSTM_{seed}^{multi}$, achieved a median NSE
 405 value of ~ 0.83 , surpassing the ~ 0.82 benchmark set by $LSTM_{seed}^{multi}$ (Table D4). This
 406 advancement was achieved through random seed variation and cross-model-type ensembling.
 407 The performance of $(LSTM + \delta HBV)_{seed}^{123}$ ensemble proved more robust than $LSTM_{seed}^{multi}$, with
 408 only a slight boost when we incorporated random seeds, i.e., $(LSTM + \delta HBV)_{seed}^{123}$. Notably,
 409 the derived $(LSTM + \delta HBV)_{seed}^{123}$ ensemble outperformed $LSTM^1$ across almost all basins

410 (Figure 4). Further incorporation of $LSTM^{multi}$ into this framework, especially when using
 411 multiple random seeds, $(LSTM + \delta HBV)^{123}_{seed} + LSTM^{multi}_{seed}$, yielded the best overall
 412 performance. Here, the margin over the previous benchmark was small in the temporal test.
 413 However, as we will show in sect. 3.2, the previous benchmark, $LSTM^{multi}_{seed}$, lacked robustness,
 414 exhibited greater deficiencies in spatial generalization, and negatively impacted ensemble
 415 simulations.

416 When we changed the number of random seeds from 3 to 10, we found that although all
 417 model and ensemble performances slightly increased, the gaps between them did not change
 418 much (Figure 5 and Table D5). In particular, the gap between $(LSTM + \delta HBV)^{123}_{seed} +$
 419 $LSTM^{multi}_{seed}$ and $(LSTM + \delta HBV)^{123}_{seed}$ or $LSTM^{multi}_{seed}$ remained unchanged. This indicates that
 420 the benefits from more random seeds rapidly become marginal, and our results based on 3
 421 random seeds were sufficiently robust. For LSTMs alone, different random seeds displayed
higher variation, and ensembling them led to greater improvement than ensembling
 $(LSTM + \delta HBV)^{123}$ with additional random seeds. It was noteworthy that while the
 424 $(LSTM + \delta HBV)^{123}$ ensemble generally showed the lowest RMSE values, it did not always
 425 show the best high flow performance, as indicated by highRMSE (Tables D1-D4). After
 426 incorporating the $LSTM^{multi}_{seed}$ variant into $(LSTM + \delta HBV)^{123}_{seed} + LSTM^{multi}_{seed}$, overall RMSE
 427 and highRMSE both improved. Nevertheless, this ensemble did not always obtain the best
 428 values in other metrics like low flow (lowRMSE) and requires further improvement.

429



432 *Figure 5. Cumulative distribution function (CDF) curves based on temporal test results for*
 433 *$LSTM^{multi}$, $(LSTM + \delta HBV)^{123}$, and $[(LSTM + \delta HBV)^{123} + LSTM^{multi}]$. The solid lines*
 434 *(with “seed”) denote the results with 10 random seeds while the corresponding dashed and*

435 translucent lines denote the performances of their individual members each based on one
 436 random seed.

437

438 3.2. Spatial generalization

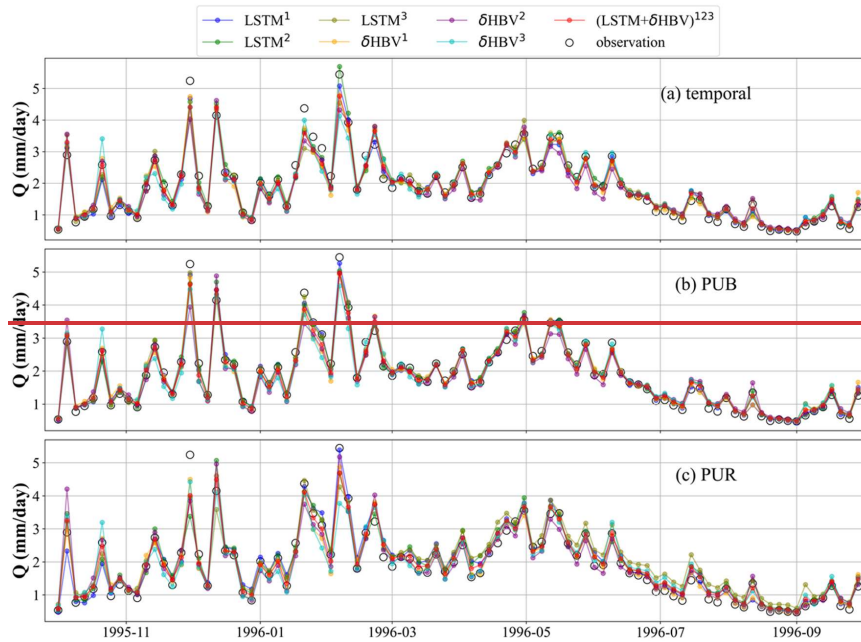
439 It is clear that cross-model-type ensembling and the incorporation of δ HBV significantly
 440 improved prediction in ungauged basins (PUB) or regions (PUR), mitigating the difficulty of
 441 spatial generalization (Figure 2b - 2c). In particular, the previous record-holder for temporal
 442 test performance, $LSTM_{seed}^{multi}$, incurred large drops in the PUB and PUR tests, once again
 443 reminding us of the limitations of LSTM in spatial generalization. Given the same forcings,
 444 δ HBV-only individual simulations or ensembles consistently outperformed LSTM-only
 445 counterparts in the PUR test. Furthermore, adding δ HBV to the same-model-type LSTM
 446 ensembles improved median NSE by 0.02-0.03 for PUB. The role of δ HBV became even more
 447 prominent in the harder PUR tests, with an increased gap (0.04-0.07), e.g., $LSTM^{123}$ (median
 448 NSE ~0.656) and $(LSTM + \delta HBV)^{123}$ (median NSE ~0.701). The increased significance of
 449 δ HBV is also illustrated by the optimized weights shown in Figure E1. The weights are, which
 450 were estimated via using a genetic algorithm using the with streamflow observations during from
 451 the test periods. Here the estimated These weights are presented solely used to display illustrate
 452 the relative contributions of the different ensemble components. The significantly different
 453 spatial distribution patterns of these weights among different test scenarios also indicate the
 454 differences among temporal, PUB, and PUR tests (Figures E2-E3). The performance of
 455 $(LSTM + \delta HBV)^{123}$ improved compared to $LSTM^{multi}$ whether or not we employed multiple
 456 random seeds to form an ensemble. As such, we can conclude that the inclusion of a
 457 differentiable process-based model like δ HBV in an ensemble is a systematic way to reduce
 458 the risks of failed generalizations of LSTM.

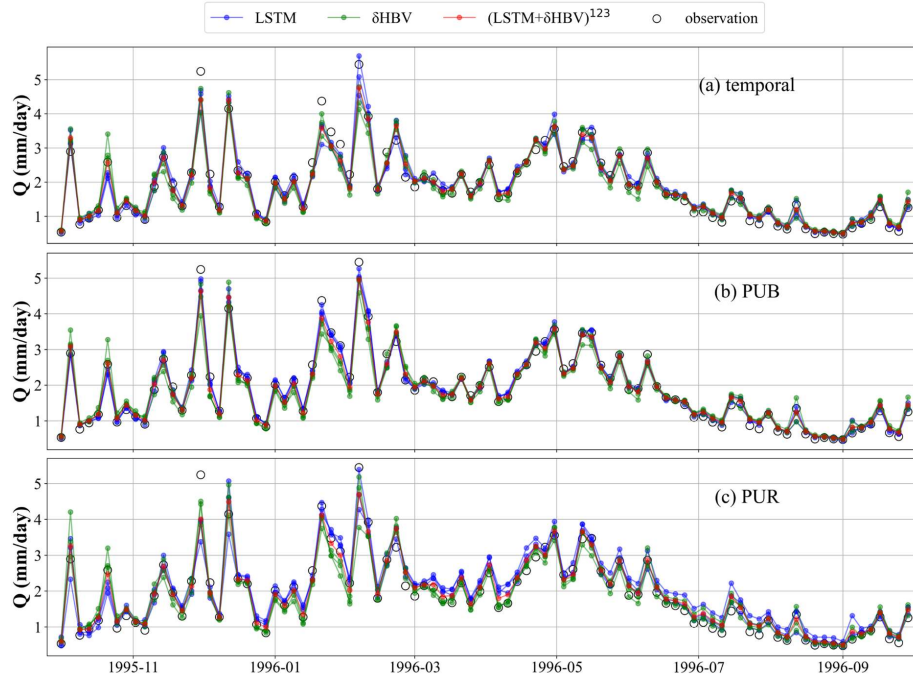
459 Utilizing a cross-model-type ensemble led to widespread improvements over LSTM-only
 460 ensembles, with the exception of a few scattered basins for each temporal -(Figure 4-a2), PUB

461 (Figure 4-b2), and PUR (Figure 4-c2) test. The most significant improvements due to the
462 ensemble were concentrated on the center of the Great Plains along with the midwestern US,
463 while the eastern US was moderately improved, suggesting data uncertainty is a larger issue in
464 the central and midwestern US. The Great Plains have historically had poor performance for
465 all kinds of models (Mai et al., 2022) and even the ensemble model had NSE values of only
466 0.3-0.4 for many of the basins there, although this still marked significant improvements over
467 LSTM¹ (Figure 4-a2, -b2, -c2). Some western basin NSE values were elevated by more than
468 0.15 for the temporal test (Figure 4-a2) and even more for PUB and PUR. Meteorological
469 stations are generally sparse on the Great Plains, and an ensemble seems to be an effective way
470 to leverage the different forcing datasets that are available. The poor performances in some
471 basins highlight some remaining deficiencies in current models, which clearly cannot fully
472 consider the heterogeneities of different basins; thus, multiscale formulations that resolve such
473 heterogeneities may have advantages (Song et al., 2024a)(Song et al., 2024a).

474 To investigate why ensembles outperformed single-model, single-forcing approaches, we
475 compared their temporal, PUB, and PUR test simulation time series against observations for
476 531 basins (Figure 6). Analysis of averaged hydrological year data revealed that while
477 individual ensemble members using single-source forcing datasets performed similarly for
478 easily simulated periods, they showed significant divergence during challenging periods,
479 particularly peak flows. This divergence stems from distinct systematic errors inherent to
480 different model types and forcing datasets. Notably, LSTM-based simulations alone proved
481 insufficient in generating adequate spread to capture these divergent points. A key finding was
482 that SHBV exhibited markedly different variation patterns compared to LSTM, and its
483 inclusion substantially increased the ensemble spread. By averaging individual model outputs
484 and stabilizing uncertainties, ensemble simulations achieved effective and robust performance
485 across all conditions, which can be shown via the metric highRMSE and lowRMSE values in

486 Tables D1-D4. This highlights the critical importance of comprehensive training for each
 487 ensemble member, including diverse forcing inputs, full-period model calibration, and rigorous
 488 hyperparameter tuning, to enable the development of ensure that each member develops
 489 distinct characteristics in their simulation behaviors. These differences allow the ensemble to
 490 better represent a range of hydrological responses, particularly under extreme or uncertain
 491 conditions. By capturing complementary strengths and compensating for individual
 492 weaknesses, such well-trained ensemble members collectively enhance the robustness and
 493 accuracy of streamflow simulations, ultimately enhancing ensemble performance.





495
496 *Figure 6. Comparisons between multi-basin-averaged streamflow observations and*
497 *simulations across 531 basins. The time series points are displayed at four-day intervals for*
498 *clarity and conciseness. Ensemble members based on the same model (LSTM or δHBV) but*
499 *driven by different forcing datasets are shown in the same color to highlight the differences*
500 *between models more clearly.*

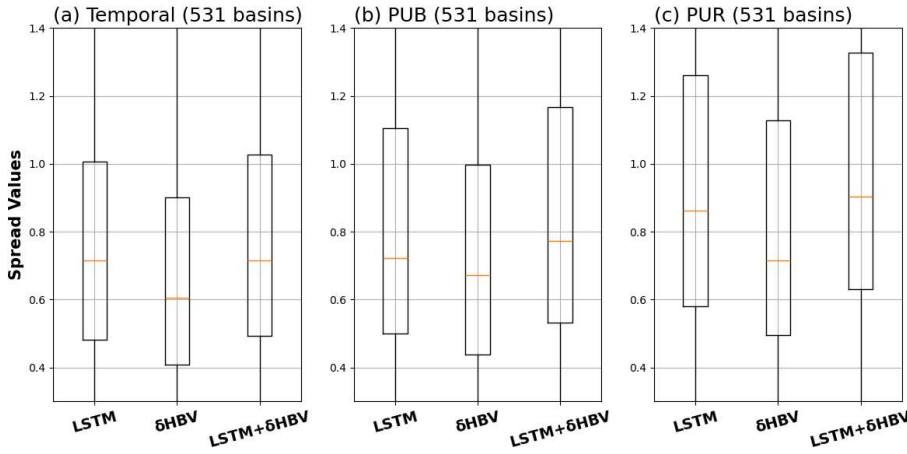
501
502 3.3 Ensemble variability and robustness analysis

503 Although δHBV (median spread 0.61) exhibits lower spreads than LSTM (mean spread
504 0.72), their combination increases the ensemble spreads, thereby enhancing diversity (Figure
505 7). This pattern holds across the temporal, PUB, and PUR tests. Ensemble effectiveness
506 depends on the diversity of model behaviors and their distinct error characteristics.
507 Consequently, larger spreads contribute to greater ensemble benefits. Figure D3 further
508 demonstrates that δHBV+LSTM exhibits larger spreads than LSTM in most basins.

← Formatted: Header

← Formatted: Font: 12 pt

← Formatted: Justified, Indent: First line: 0.33"



509
510 *Figure 7. Spread values (Table C2) of each model for LSTM, δ HBV, and LSTM + δ HBV due*
511 *to different meteorological forcings and random seeds across temporal, PUB, and PUR tests.*

512
513 As the warming signal is already clear across most basins under any forcing across the
514 periods of simulation (Figure D4), the models' strong performance in the temporal test suggests
515 decent extrapolation capability under warming scenarios. It is often questioned whether data-
516 driven models like LSTM lose accuracy under stronger climate drift, but no substantially
517 warmed dataset is available to test this. Benchmarks suggest LSTM captures 15-year trends
518 well in temporal tests, but less so in data-sparse scenarios (Feng et al., 2023b). Introducing a
519 10% precipitation perturbation (multiplying precipitation by 1.1) slightly reduced performance
520 for both models as expected (Figures D5a and D5b), but ensemble benefits remained robust
521 across models despite the perturbation.

522 Training sample size, dynamic parameter choices, and lookback windows all have limited
523 impact on our conclusions. δ HBV shows limited sensitivity to sample size, with similar results
524 when trained on 531 versus 671 basins (Figure D5c). Regarding parameter uncertainties, fixing
525 one δ HBV parameter (k_0) as static increased structural errors and reduced performance (Figure
526 D5d), yet ensemble benefits remained robust. For LSTM, alternative window sizes of 182 and

527 730 days were tested, with the default 365-day window yielding optimal performance (Figure
 528 D5e). Importantly, variations in the lookback window had only minor effects on model
 529 performance, underscoring the robustness of ensemble benefits.

530
 531 3.4. Further discussion

532 Based on our results, we identified several avenues for future research ~~directions~~. First,
 533 while we have explored various weighting strategies and found that averaging yields the best
 534 performance yet, we believe that dynamic or adaptive weighting schemes could further enhance
 535 performance in future studies. It is also demonstrated by Table E1 that estimated uneven
 536 weights can significantly improve simulation performance. Moreover, within specific basins,
 537 the estimated weights of different components are often highly imbalanced, as evidenced by
 538 the spatial distribution of optimized weights (Figures E2-E3). Some potential feasible ways
 539 include using the simulations from these individual-individually-trained models as inputs of a
 540 data-driven model (Solanki et al., 2025), and making the weight estimation and the ensemble
 541 member training simultaneously.

542 Both LSTM and δ HBV models exhibit limitations in regions with significant
 543 anthropogenic impacts like dam presence, as well as arid climatic and significantly
 544 heterogeneous geological conditions. These regions are mainly located in the midwestern and
545 western CONUS, where high evaporation conditions (Heidari et al., 2020, Figure 2) and
546 numerous dams (Ryan Bellmore et al., 2017, Figure 1) coincide with complex water use
547 processes (Wada et al., 2016, Figure 11) that current models cannot simulate well. Together,
548 these factors suggest that anthropogenic influence is likely an important driver of poor model
549 performance. Further improvements may include incorporating additional data that capture
 550 these factors like capacity-to-runoff ratio (Ouyang et al., 2021)(Ouyang et al., 2021) or
 551 integrating specialized modules, such as reservoirs (Hanazaki et al., 2022; West et al., 2025).
 552 Compared with LSTM, δ HBV is more sensitive to precipitation biases. For example, the

← Formatted: Header

553 differences between δ HBV simulations under different forcing datasets were generally larger
554 than those for LSTM, and δ HBV using the Daymet forcing dataset showed largely better
555 performance than with the other two forcing datasets, which indicates that δ HBV may not be
556 able to fit different forcing datasets well. Therefore, many potential structural optimizations
557 can be implemented to improve δ HBV. Our analysis provided corroborating evidence that
558 forcing error is an important reason why LSTM can outperform δ HBV in the temporal test for
559 some basins, although such patterns may not generalize well in space. A meteorological forcing
560 data correction module can be developed in the future to account for timing and magnitude
561 errors in precipitation. ~~Moreover, ensemble simulations may face challenges when
562 computational resources are limited and calculations are performed sequentially. However, we
563 remain optimistic about these challenges, as the processes can be addressed by leveraging
564 parallel computing with multiple GPUs, benefiting from ongoing advancements in
565 computational power~~ Ensemble simulations may face challenges when computational resources
566 are constrained, particularly for large-scale or real-time applications. Nevertheless, we remain
567 optimistic about overcoming these challenges due to several promising solutions. These
568 include tailoring the hydrological model by simplifying less relevant components to specific
569 simulation objectives (Clark et al., 2015; Kraft et al., 2022) and cloud-based computing
570 infrastructures that offer scalable, on-demand resource allocation (He et al., 2024; Leube et al.,
571 2013). Importantly, the majority of computational costs are incurred during model training. In
572 practice, ensemble members are typically pre-trained by different research or application
573 groups (Bodnar et al., 2025; Nearing et al., 2024; Song et al., 2025a), enabling direct reuse of
574 these well-trained models and significantly improving computational efficiency.

← Formatted: Font: 13 pt

575 For this work, we did not create a δ HBV^{multi} model (in the same vein as LSTM^{multi}) using
576 all forcings as an input to a single model, since a similar experiment has already been conducted
577 by Sawadekar et al. (2025). We also did not examine “seed” combinations of a δ HBV^{multi} as

← Formatted: Header

578 we believed they would not result in a significant performance boost (unlike that seen with
579 $LSTM^{multi}$), because LSTM has high variability and low bias, while δHBV has lower variance
580 and potentially higher bias. As a result, random seeds would likely not create large enough
581 perturbations for δHBV and wouldn't bring the benefits seen with $LSTM_{seed}^{multi}$. To achieve an
582 equivalent perturbation level for δHBV , it may be necessary to incorporate multiple distinct
583 hydrological models, such as SAC-SMA, PRMS, and GR4J, similar to the approach
584 implemented in the Framework for Understanding Structural Errors (FUSE) (Clark et al., 2008).
585 Work is ongoing to create a combination of a series of differentiable process-based models,
586 which is expected to produce a further improved ensemble with great interpretability. Given
587 the success of cross-model-type ensembles shown in this work, we also encourage further
588 exploration of ensemble simulations involving models with other distinct mechanisms.
589

590 **4. Summary and Conclusions**

Formatted: Font color: Auto

Formatted: Font color: Auto

591 This study comprehensively analyzes ensemble combinations of two advanced model
592 types (LSTM and δHBV), each with distinct mechanisms, for streamflow simulation across
593 531 basins in the US. Three meteorological forcing datasets (Daymet, NLDAS, and Maurer)
594 are employed to fully capture the characteristics of the two models, ~~and their applications in~~
595 ~~two different ways are also tested. Their applications are also tested in two distinct ways: (1)~~
596 ~~by feeding all diverse forcing datasets simultaneously into a single LSTM model, and (2) by~~
597 ~~ensembling the outputs of multiple LSTM models, each trained separately using a single~~
598 ~~forcing dataset.~~ The performance of ensemble simulations was evaluated under three distinct
599 testing scenarios (temporal, PUB, and PUR tests), surpassing the previous highest
600 performances. Our findings enhance the understanding of how to effectively utilize diverse
601 model types and multi-source datasets to improve streamflow simulations. The principal
602 conclusions are:

← Formatted: Header

Formatted: Indent: Hanging: 0.27", Outline numbered +
Level: 1 + Numbering Style: 1, 2, 3, ... + Start at: 1 +
Alignment: Left + Aligned at: 0.33" + Indent at: 0.6"

603 (1) Cross-model-type ensembles (LSTM+ δ HBV) consistently outperformed single-
604 model approaches across all test scenarios, setting new performance benchmarks on
605 the CAMELS dataset. These ensembles demonstrated the complementarity of data-
606 driven (LSTM) and physics-informed (δ HBV) approaches in capturing diverse
607 hydrological behaviors.

608 (2) Ensembling models trained on different forcing datasets proved more effective than
609 using multiple forcing datasets as simultaneous inputs to a single model. This suggests
610 that separate training allows each model to capture unique features contained in each
611 forcing dataset, which can then be effectively leveraged in the ensemble.

612 (3) δ HBV provided significant benefits to ensemble simulations on spatial generalization.
613 Ensembling LSTM with δ HBV showed increasing benefits as generalization
614 challenges increased, from temporal to spatial interpolation (PUB) to spatial
615 extrapolation (PUR) tests. This underscores the value of physics-informed constraints
616 in improving model transferability to ungauged basins and regions.

617 (4) While ensemble methods significantly improved overall performance, they did not
618 fully mitigate consistent deficiencies in certain challenging areas (e.g., regions with
619 high dam density or heterogeneous hydrogeological conditions). This indicates areas
620 for future model development.

621 These findings have important implications for hydrological modeling and water
622 resources management. The improved accuracy and spatial generalization of our ensemble
623 approach can enhance streamflow predictions, benefiting water resources planning and
624 management, particularly in data-scarce regions. Our results also suggest that future
625 hydrological model development should focus on combining data-driven and physics-based
626 approaches to improve model generalizability across diverse conditions. The superior
627 performance of ensembling models with different forcing datasets over using merged forcings

628 as a single input highlights the risk of indiscriminately feeding all available data into one data-
629 driven model. While computational demands certainly require consideration, the potential
630 improvements in prediction accuracy offer significant value for both research and operational
631 applications. Future work should focus on refining these ensemble techniques, addressing
632 model limitations in challenging regions, and exploring ensemble implementation in
633 operational settings.

634 **Code and data availability**

Formatted: Header

Formatted: Font color: Auto

635 The source codes and datasets utilized in this study are publicly accessible through the
636 following repositories: The SHBV modeling framework, including all computational scripts
637 and documentation, is hosted on Zenodo (<https://doi.org/10.5281/zenodo.7091334>) (Feng et al.,
638 2023a), with an updated version and comprehensive software release scheduled upon
639 manuscript acceptance. The implementation of the LSTM architecture is accessible through
640 Zenodo (<https://doi.org/10.5281/zenodo.6326394>) (Kratzert et al., 2022). The CAMELS
641 hydrometeorological dataset, which provides the foundational basin characteristics and time
642 series data used in our analysis, can be obtained via <https://dx.doi.org/10.5065/D6MW2F4D>
643 (Addor et al., 2017; Newman and Clark, 2014).

644

645 **Author contributions**

Formatted: Font color: Auto

646 PL and CS designed the experiments and PL carried them out. YS developed the modified
647 SHBV code. PL prepared the manuscript with contributions from all co-authors.

648

649 **Competing interests**

Formatted: Font color: Auto

650 Chaopeng Shen and Kathryn Lawson have financial interests in HydroSapient, Inc., a
651 company that could potentially benefit from the results of this research. This interest has been
652 reviewed by the Pennsylvania State University in accordance with its individual conflict of
653 interest policy for the purpose of maintaining the objectivity and the integrity of research. The
654 other authors have no competing interests to declare.

655

656 **Acknowledgments**

Formatted: Font color: Auto

657 PL, CS, and KL were supported by the Office of Biological and Environmental Research
658 of the U.S. Department of Energy (contract no. DESC0016605). PJ and MP were also partially

659 supported by California Department of Water Resources Atmospheric River Program Phase III
 660 (Grant 4600014294). YS and CS were partially supported by subaward A23-0252-S002 from
 661 the Cooperative Institute for Research to Operations in Hydrology (CIROH) through the
 662 National Oceanic and Atmospheric Administration (NOAA) Cooperative Agreement (Grant
 663 no. NA22NWS4320003).

664

665 **References**

666 Aboelyazeed, D., Xu, C., Hoffman, F. M., Liu, J., Jones, A. W., Rackauckas, C., Lawson,
 667 K., and Shen, C.: A differentiable, physics informed ecosystem modeling and learning
 668 framework for large scale inverse problems: demonstration with photosynthesis simulations,
 669 *Biogeosciences*, 20, 2671–2692, <https://doi.org/10.5194/bg-20-2671-2023>, 2023.

670 Addor, N., Newman, A. J., Mizukami, N., and Clark, M. P.: The CAMELS data set:
 671 catchment attributes and meteorology for large sample studies, *Hydrol. Earth Syst. Sci.*, 21,
 672 5293–5313, <https://doi.org/10.5194/hess-21-5293-2017>, 2017.

673 Aghakouchak, A. and Habib, E.: Application of a Conceptual Hydrologic Model in
 674 Teaching Hydrologic Processes, *International Journal of Engineering Education*, 26, 2010.

675 Bandai, T. and Ghezzehei, T. A.: Physics informed neural networks with monotonicity
 676 constraints for Richardson–Richards equation: Estimation of constitutive relationships and soil
 677 water flux density from volumetric water content measurements, *Water Resources Research*,
 678 57, e2020WR027642, <https://doi.org/10.1029/2020wr027642>, 2021.

679 Beek, H. E., van Dijk, A. I. J. M., de Roo, A., Dutra, E., Fink, G., Orth, R., and Schellekens,
 680 J.: Global evaluation of runoff from 10 state-of-the-art hydrological models, *Hydrology and*
 681 *Earth System Sciences*, 21, 2881–2903, <https://doi.org/10.5194/hess-21-2881-2017>, 2017.

682 Beek, H. E., Pan, M., Lin, P., Seibert, J., Dijk, A. I. J. M. van, and Wood, E. F.: Global
 683 fully distributed parameter regionalization based on observed streamflow from 4,229

684 headwater catchments, *Journal of Geophysical Research: Atmospheres*, 125, e2019JD031485,
685 <https://doi.org/10.1029/2019JD031485>, 2020.

686 Behnke, R., Vavrus, S., Allstadt, A., Albright, T., Thogmartin, W. E., and Radeloff, V. C.:
687 Evaluation of downscaled, gridded climate data for the conterminous United States, *Ecological
688 Applications*, 26, 1338–1351, <https://doi.org/10.1002/15-1061>, 2016.

689 Bell, V. A. and Moore, R. J.: The sensitivity of catchment runoff models to rainfall data
690 at different spatial scales, *Hydrology and Earth System Sciences*, 4, 653–667,
691 <https://doi.org/10.5194/hess-4-653-2000>, 2000.

692 Bergström, S.: Development and application of a conceptual runoff model for
693 Scandinavian catchments, PhD Thesis, Swedish Meteorological and Hydrological Institute
694 (SMHI), Norköping, Sweden, 1976.

695 Bergström, S.: The HBV model – its structure and applications, SMHI, 1992.

696 Bindas, T., Tsai, W. P., Liu, J., Rahmani, F., Feng, D., Bian, Y., Lawson, K., and Shen,
697 C.: Improving river routing using a differentiable Muskingum-Cunge model and physics-
698 informed machine learning, *Water Resources Research*, 60, e2023WR035337,
699 <https://doi.org/10.1029/2023WR035337>, 2024.

700 Brunner, M. I., Slater, L., Tallaksen, L. M., and Clark, M.: Challenges in modeling and
701 predicting floods and droughts: A review, *WIREs Water*, 8, e1520,
702 <https://doi.org/10.1002/wat2.1520>, 2021.

703 Clark, M. P., Slater, A. G., Rupp, D. E., Woods, R. A., Vrugt, J. A., Gupta, H. V., Wagener,
704 T., and Hay, L. E.: Framework for Understanding Structural Errors (FUSE): A modular
705 framework to diagnose differences between hydrological models, *Water Resources Research*,
706 44, <https://doi.org/10.1029/2007WR006166>, 2008.

707 Clark, M. P., Wilby, R. L., Gutmann, E. D., Vano, J. A., Gangopadhyay, S., Wood, A. W.,
708 Fowler, H. J., Prudhomme, C., Arnold, J. R., and Brekke, L. D.: Characterizing uncertainty of

709 the hydrologic impacts of climate change, *Curr. Clim. Change. Rep.*, 2, 55–64,
710 <https://doi.org/10.1007/s40641-016-0034-x>, 2016.

711 Dion, P., Martel, J. L., and Arsenault, R.: Hydrological ensemble forecasting using a
712 multi-model framework, *Journal of Hydrology*, 600, 126537,
713 <https://doi.org/10.1016/j.jhydrol.2021.126537>, 2021.

714 Feng, D., Fang, K., and Shen, C.: Enhancing streamflow forecast and extracting insights
715 using long short-term memory networks with data integration at continental scales, *Water
716 Resources Research*, 56, e2019WR026793, <https://doi.org/10.1029/2019WR026793>, 2020.

717 Feng, D., Lawson, K., and Shen, C.: Mitigating prediction error of deep learning
718 streamflow models in large data sparse regions with ensemble modeling and soft data,
719 *Geophysical Research Letters*, 48, e2021GL092999, <https://doi.org/10.1029/2021GL092999>,
720 2021.

721 Feng, D., Liu, J., Lawson, K., and Shen, C.: Differentiable, learnable, regionalized
722 process-based models with multiphysical outputs can approach state-of-the-art hydrologic
723 prediction accuracy, *Water Resources Research*, 58, e2022WR032404,
724 <https://doi.org/10.1029/2022WR032404>, 2022.

725 Feng, D., Shen, C., Liu, J., Lawson, K., and Beck, H.: differentiable parameter learning
726 (dPL) + HBV hydrologic model, <https://doi.org/10.5281/zenodo.7943626>, 2023a.

727 Feng, D., Beck, H., Lawson, K., and Shen, C.: The suitability of differentiable, physics-
728 informed machine learning hydrologic models for ungauged regions and climate change impact
729 assessment, *Hydrology and Earth System Sciences*, 27, 2357–2373,
730 <https://doi.org/10.5194/hess-27-2357-2023>, 2023b.

731 Hanazaki, R., Yamazaki, D., and Yoshimura, K.: Development of a reservoir flood control
732 scheme for global flood models, *JAMES*, 14, e2021MS002944,
733 <https://doi.org/10.1029/2021MS002944>, 2022.

734 Hargreaves, G. H.: Defining and using reference evapotranspiration, *Journal of Irrigation*
735 and Drainage Engineering, 120, 1132–1139, [https://doi.org/10.1061/\(ASCE\)0733-9437\(1994\)120:6\(1132\)](https://doi.org/10.1061/(ASCE)0733-9437(1994)120:6(1132)), 1994.

737 Hechreiter, S. and Schmidhuber, J.: Long Short Term Memory, *Neural Computation*, 9,
738 1735–1780, <https://doi.org/10.1162/neco.1997.9.8.1735>, 1997.

739 Jiang, S., Zheng, Y., and Solomatine, D.: Improving AI system awareness of geoscience
740 knowledge: Symbiotic integration of physical approaches and deep learning, *Geophysical*
741 *Research Letters*, 47, e2020GL088229, <https://doi.org/10.1029/2020GL088229>, 2020.

742 Kling, H., Fuchs, M., and Paulin, M.: Runoff conditions in the upper Danube basin under
743 an ensemble of climate change scenarios, *Journal of Hydrology*, 424–425, 264–277,
744 <https://doi.org/10.1016/j.jhydrol.2012.01.011>, 2012.

745 Kraft, B., Jung, M., Körner, M., Keirala, S., and Reichstein, M.: Towards hybrid modeling
746 of the global hydrological cycle, *Hydrology and Earth System Sciences*, 26, 1579–1614,
747 <https://doi.org/10.5194/hess-26-1579-2022>, 2022.

748 Kratzert, F., Klotz, D., Brenner, C., Schulz, K., and Herrnegger, M.: Rainfall Runoff
749 modelling using Long Short-Term Memory (LSTM) networks, *Hydrology and Earth System
750 Sciences*, 22, 6005–6022, <https://doi.org/10.17605/OSF.IO/QV5JZ>, 2018.

751 Kratzert, F., Klotz, D., Herrnegger, M., Sampson, A. K., Hochreiter, S., and Nearing, G.
752 S.: Toward improved predictions in ungauged basins: Exploiting the power of machine learning,
753 *Water Resources Research*, 55, 11344–11354, <https://doi.org/10.1029/2019WR025482>, 2019.

754 Kratzert, F., Klotz, D., Hochreiter, S., and Nearing, G. S.: A note on leveraging synergy
755 in multiple meteorological data sets with deep learning for rainfall runoff modeling, *Hydrology
756 and Earth System Sciences*, 25, 2685–2703, <https://doi.org/10.5194/hess-25-2685-2021>, 2021.

757 Kratzert, F., Gauch, M., Nearing, G., and Klotz, D.: NeuralHydrology – A Python library
758 for Deep Learning research in hydrology, <https://doi.org/10.5281/zenodo.6326394>, 2022.

759 Li, P., Zha, Y., Shi, L., Tso, C. H. M., Zhang, Y., and Zeng, W.: Comparison of the use
760 of a physical-based model with data assimilation and machine learning methods for simulating
761 soil water dynamics, Journal of Hydrology, 584, 124692,
762 <https://doi.org/10.1016/j.jhydrol.2020.124692>, 2020a.

763 Li, P., Zha, Y., Tso, C. H. M., Shi, L., Yu, D., Zhang, Y., and Zeng, W.: Data assimilation
764 of uncalibrated soil moisture measurements from frequency domain reflectometry, Geoderma,
765 374, 114432, <https://doi.org/10.1016/j.geoderma.2020.114432>, 2020b.

766 Li, P., Zha, Y., Zuo, B., and Zhang, Y.: A family of soil water retention models based on
767 sigmoid functions, Water Resources Research, 59, e2022WR033160,
768 <https://doi.org/10.1029/2022WR033160>, 2023a.

769 Li, P., Zha, Y., and Tso, C. H. M.: Reconstructing GRACE derived terrestrial water
770 storage anomalies with in situ groundwater level measurements and meteorological forcing
771 data, Journal of Hydrology: Regional Studies, 50, 101528,
772 <https://doi.org/10.1016/j.ejrh.2023.101528>, 2023b.

773 Li, P., Zha, Y., Zhang, Y., Michael Tso, C. H., Attinger, S., Samaniego, L., and Peng, J.:
774 Deep learning integrating scale conversion and pedo-transfer function to avoid potential errors
775 in cross scale transfer, Water Resources Research, 60, e2023WR035543,
776 <https://doi.org/10.1029/2023WR035543>, 2024.

777 Lin, Y., Wang, D., Zhu, J., Sun, W., Shen, C., and Shangguan, W.: Development of
778 objective function based ensemble model for streamflow forecasts, Journal of Hydrology, 632,
779 130861, <https://doi.org/10.1016/j.jhydrol.2024.130861>, 2024.

780 Lins, H. F. and Slack, J. R.: Streamflow trends in the United States, Geophysical Research
781 Letters, 26, 227–230, <https://doi.org/10/d5zb6d>, 1999.

782 Liu, J., Rahmani, F., Lawson, K., and Shen, C.: A multiscale deep learning model for soil
783 moisture integrating satellite and in situ data, Geophysical Research Letters, 49,

784 e2021GL096847, <https://doi.org/10.1029/2021GL096847>, 2022.

785 Liu, J., Bian, Y., Lawson, K., and Shen, C.: Probing the limit of hydrologic predictability
786 with the Transformer network, *Journal of Hydrology*, 637, 131389,
787 <https://doi.org/10.1016/j.jhydrol.2024.131389>, 2024.

788 Mai, J., Craig, J. R., Tolson, B. A., and Arsenault, R.: The sensitivity of simulated
789 streamflow to individual hydrologic processes across North America, *Nat Commun*, 13, 455,
790 <https://doi.org/10.1038/s41467-022-28010-7>, 2022.

791 Maurer, E. P., Wood, A. W., Adam, J. C., Lettenmaier, D. P., and Nijssen, B.: A long-
792 term hydrologically based dataset of land surface fluxes and states for the conterminous United
793 States, *Journal of Climate*, 15, 3237–3251, [https://doi.org/10.1175/1520-0442\(2002\)015<3237:ALTHBD>2.0.CO;2](https://doi.org/10.1175/1520-0442(2002)015<3237:ALTHBD>2.0.CO;2), 2002.

795 Moges, E., Demissie, Y., and Li, H. Y.: Hierarchical mixture of experts and diagnostic
796 modeling approach to reduce hydrologic model structural uncertainty, *Water Resources
797 Research*, 52, 2551–2570, <https://doi.org/10.1002/2015WR018266>, 2016.

798 Nai, C., Liu, X., Tang, Q., Liu, L., Sun, S., and Gaffney, P. P. J.: A novel strategy for
799 automatic selection of cross-basin data to improve local machine learning-based runoff models,
800 *Water Resources Research*, 60, e2023WR035051, <https://doi.org/10.1029/2023WR035051>,
801 2024.

802 Narkhede, M. V., Bartakke, P. P., and Sutaone, M. S.: A review on weight initialization
803 strategies for neural networks, *Artificial Intelligence Review*, 55, 291–322,
804 <https://doi.org/10.1007/s10462-021-10033-z>, 2022.

805 Nash, J. E. and Sutcliffe, J. V.: River flow forecasting through conceptual models part I
806 — A discussion of principles, *Journal of Hydrology*, 10, 282–290,
807 [https://doi.org/10.1016/0022-1694\(70\)90255-6](https://doi.org/10.1016/0022-1694(70)90255-6), 1970.

808 Nearing, G., Cohen, D., Dube, V., Gauch, M., Gilon, O., Harrigan, S., Hassidim, A., Klotz,

809 D., Kratzert, F., Metzger, A., Nevo, S., Pappenberger, F., Prudhomme, C., Shalev, G., Shenzis,
810 S., Tekalign, T. Y., Weitzner, D., and Matias, Y.: Global prediction of extreme floods in
811 ungauged watersheds, *Nature*, 627, 559–563, <https://doi.org/10.1038/s41586-024-07145-1>,
812 2024.

813 Newman, A. J. and Clark, M.: A large sample watershed scale hydrometeorological
814 dataset for the contiguous USA, <https://doi.org/10.5065/D6MW2F4D>, 2014.

815 Newman, A. J., Mizukami, N., Clark, M. P., Wood, A. W., Nijssen, B., Nearing, G.,
816 Newman, A. J., Mizukami, N., Clark, M. P., Wood, A. W., Nijssen, B., and Nearing, G.:
817 Benchmarking of a Physically Based Hydrologic Model, *Journal of Hydrometeorology*, 18,
818 2215–2225, <https://doi.org/10/gbwr9s>, 2017.

819 Newman, A. J., Clark, M. P., Longman, R. J., and Giambelluca, T. W.: Methodological
820 intercomparisons of station-based gridded meteorological products: Utility, limitations, and
821 paths forward, <https://doi.org/10.1175/JHM-D-18-0114.1>, 2019.

822 Ouyang, W., Lawson, K., Feng, D., Ye, L., Zhang, C., and Shen, C.: Continental-scale
823 streamflow modeling of basins with reservoirs: Towards a coherent deep learning-based
824 strategy, *Journal of Hydrology*, 599, 126455, <https://doi.org/10.1016/j.jhydrol.2021.126455>,
825 2021.

826 Paul, P. K., Zhang, Y., Ma, N., Mishra, A., Panigrahy, N., and Singh, R.: Selecting
827 hydrological models for developing countries: Perspective of global, continental, and country
828 scale models over catchment scale models, *Journal of Hydrology*, 600, 126561,
829 <https://doi.org/10.1016/j.jhydrol.2021.126561>, 2021.

830 Rahmani, F., Appling, A., Feng, D., Lawson, K., and Shen, C.: Identifying structural
831 priors in a hybrid differentiable model for stream water temperature modeling, *Water
832 Resources Research*, 59, e2023WR034420, <https://doi.org/10.1029/2023WR034420>, 2023.

833 Sawadekar, K., Song, Y., Pan, M., Beck, H., McCrary, R., Ullrich, P., Lawson, K., and

834 Shen, C.: Hydrology Informed Interpretable Precipitation Data Fusion with a Differentiable
835 Hydrologic Model, <https://doi.org/10.2139/ssrn.4967007>, 25 September 2024.

836 Shen, C., Appling, A. P., Gentine, P., Bandai, T., Gupta, H., Tartakovsky, A., Baity-Jesi,
837 M., Fenicia, F., Kifer, D., Li, L., Liu, X., Ren, W., Zheng, Y., Harman, C. J., Clark, M., Farthing,
838 M., Feng, D., Kumar, P., Aboelyazeed, D., Rahmani, F., Song, Y., Beek, H. E., Bindas, T.,
839 Dwivedi, D., Fang, K., Höge, M., Rackauckas, C., Mohanty, B., Roy, T., Xu, C., and Lawson,
840 K.: Differentiable modelling to unify machine learning and physical models for geosciences,
841 *Nat Rev Earth Environ*, 4, 552–567, <https://doi.org/10.1038/s43017-023-00450-9>, 2023.

842 Solanki, H., Vegad, U., Kushwaha, A., and Mishra, V.: Improving Streamflow Prediction
843 Using Multiple Hydrological Models and Machine Learning Methods, *Water Resources*
844 *Research*, 61, e2024WR038192, <https://doi.org/10.1029/2024WR038192>, 2025.

845 Song, Y., Bindas, T., Shen, C., Ji, H., Knoben, W. J. M., Lenzarich, L., Clark, M. P., Liu,
846 J., van Werkhoven, K., Lemont, S., Denno, M., Pan, M., Yang, Y., Rapp, J., Kumar, M.,
847 Rahmani, F., Thébault, C., Sawadekar, K., and Lawson, K.: High-resolution national-scale
848 water modeling is enhanced by multiscale differentiable physics informed machine learning,
849 <https://doi.org/10.22541/essoar.172736277.74497104/v1>, 26 September 2024a.

850 Song, Y., Sawadekar, K., Frame, J. M., Pan, M., Clark, M., Knoben, W. J. M., Wood, A.
851 W., Patel, T., and Shen, C.: Improving physics informed, differentiable hydrologic models for
852 capturing unseen extreme events, <https://doi.org/10.22541/essoar.172304428.82707157/v1>,
853 2024b.

854 Song, Y., Knoben, W. J. M., Clark, M. P., Feng, D., Lawson, K., Sawadekar, K., and Shen,
855 C.: When ancient numerical demons meet physics informed machine learning: adjoint based
856 gradients for implicit differentiable modeling, *Hydrology and Earth System Sciences*, 28,
857 3051–3077, <https://doi.org/10.5194/hess-28-3051-2024>e.

858 Thornton, P. E., Running, S. W., and White, M. A.: Generating surfaces of daily

859 meteoreological variables over large regions of complex terrain, *Journal of Hydrology*, 190,
860 214–251, [https://doi.org/10.1016/S0022-1694\(96\)03128-9](https://doi.org/10.1016/S0022-1694(96)03128-9), 1997.

861 Tsai, W. P., Feng, D., Pan, M., Beck, H., Lawson, K., Yang, Y., Liu, J., and Shen, C.:
862 From calibration to parameter learning: Harnessing the scaling effects of big data in
863 geoscientific modeling, *Nat Commun*, 12, 5988, <https://doi.org/10.1038/s41467-021-26107-z>,
864 2021.

865 Wang, N., Zhang, D., Chang, H., and Li, H.: Deep learning of subsurface flow via theory-
866 guided neural network, *Journal of Hydrology*, 584, 124700,
867 <https://doi.org/10.1016/j.jhydrol.2020.124700>, 2020.

868 West, B. D., Maxwell, R. M., and Condon, L. E.: A scalable and modular reservoir
869 implementation for large scale integrated hydrologic simulations, *Hydrology and Earth System
870 Sciences*, 29, 245–259, <https://doi.org/10.5194/hess-29-245-2025>, 2025.

871 Xia, Y., Mitchell, K., Ek, M., Sheffield, J., Cosgrove, B., Wood, E., Luo, L., Alonge, C.,
872 Wei, H., Meng, J., Livneh, B., Lettenmaier, D., Koren, V., Duan, Q., Mo, K., Fan, Y., and
873 Mocko, D.: Continental scale water and energy flux analysis and validation for the North
874 American Land Data Assimilation System project phase 2 (NL-DAS-2): 1. Intercomparison and
875 application of model products, *Journal of Geophysical Research: Atmospheres*, 117,
876 <https://doi.org/10.1029/2011JD016048>, 2012.

877 Xie, K., Liu, P., Zhang, J., Han, D., Wang, G., and Shen, C.: Physics guided deep learning
878 for rainfall runoff modeling by considering extreme events and monotonic relationships,
879 *Journal of Hydrology*, 603, 127043, <https://doi.org/10.1016/j.jhydrol.2021.127043>, 2021.

880 Yao, L., Libera, D. A., Kheimi, M., Sankarasubramanian, A., and Wang, D.: The roles of
881 climate forcing and its variability on streamflow at daily, monthly, annual, and long-term scales,
882 *Water Resources Research*, 56, e2020WR027111, <https://doi.org/10.1029/2020WR027111>,
883 2020.

884 Yilmaz, K. K., Gupta, H. V., and Wagener, T.: A process based diagnostic approach to
885 model evaluation: Application to the NWS distributed hydrologic model, *Water Resources*
886 *Research*, 44, <https://doi.org/10/fpvsgb>, 2008.

887 Yu, D., Yang, J., Shi, L., Zhang, Q., Huang, K., Fang, Y., and Zha, Y.: On the uncertainty
888 of initial condition and initialization approaches in variably saturated flow modeling,
889 *Hydrology and Earth System Sciences*, 23, 2897–2914, <https://doi.org/10.5194/hess-23-2897-2019>, 2019.

890 Yu, M., Huang, Q., and Li, Z.: Deep learning for spatiotemporal forecasting in Earth
891 system science: a review, *International Journal of Digital Earth*, 17, 2391952,
892 <https://doi.org/10.1080/17538947.2024.2391952>, 2024.

893 Zhang, Q., Shi, L., Holzman, M., Ye, M., Wang, Y., Carmona, F., and Zha, Y.: A dynamic
894 data driven method for dealing with model structural error in soil moisture data assimilation,
895 *Advances in Water Resources*, 132, 103407, <https://doi.org/10.1016/j.advwatres.2019.103407>,
896 2019.

897 Zounemat-Kermani, M., Batelaan, O., Fadaee, M., and Hinkelmann, R.: Ensemble
898 machine learning paradigms in hydrology: A review, *Journal of Hydrology*, 598, 126266,
899 <https://doi.org/10.1016/j.jhydrol.2021.126266>, 2021.

900

901

902 **Appendix A: Detailed processes of HBV employed in this study.**

903 The Hydrologiska Byrån Vattenbalansavdelning (HBV) model (Aghakouchak
 904 and Habib, 2010; Beck et al., 2020; Bergström, 1976, 1992) is a simple but effective bucket-
 905 type hydrologic model that simulates hydrologic variables including snow water equivalent,
 906 soil water, groundwater storage, evapotranspiration, quick flow, baseflow, and total streamflow.
 907 In the following texts, we describe these processes in detail by equations, in which uppercase
 908 letters indicate state variables, and lowercase letters indicate model parameters. In general, the
 909 water balance is developed based on Equation (S1).

$$EP - AE - Q_t = SN + SM + UR + LR + LAKE \quad (S1)$$

910 where EP is effective precipitation, AE is the actual evapotranspiration, Q_t is the total
 911 simulated runoff, SN is snow, SM is soil water storage, UR is the upper reservoir water level,
 912 LR is the lower reservoir water level, and $LAKE$ is the lake level (omitted in this study). First,
 913 EP is separated into liquid (RN) and solid (SN) components based on the temperature (T)
 914 relative to the threshold temperature (tt) as

$$RN = EP \text{ if } T \geq tt \quad (S2)$$

$$SN = EP \text{ if } T < tt \quad (S3)$$

915 Snow (SN) accumulates in the snowpack (SNP), while the snowmelt (SNM) is calculated using
 916 a temperature-dependent melt rate (cfm). The snowmelt (SNM) is limited to the available
 917 snowpack (SNP), and any excess melt contributes to meltwater (MW) as

$$SNP = SNP + SN \quad (S4)$$

$$SNM = \begin{cases} SNP & cfm \cdot (T - tt) \geq SNP \\ cfm \cdot (T - tt) & T \geq tt, cfm \cdot (T - tt) < SNP \\ 0 & T < tt \end{cases} \quad (S5)$$

$$MW = MW + SNM \quad (S6)$$

$$SNP = SNP - SNM \quad (S7)$$

918 Some of this meltwater (MW) refreezes based on a refreezing parameter (cfr) and the
 919 temperature difference from the threshold, returning to the snowpack (SNP). The amount of
 920 refrozen water is labeled as RFZ .

$$RFZ = \begin{cases} MW & cfr \cdot cfm \cdot (tt - T) \geq MW \\ cfr \cdot cfm \cdot (tt - T) & T < tt, cfr \cdot cfm \cdot (tt - T) < MW \\ 0 & T \geq tt \end{cases} \quad (S8)$$

$$SNP = SNP + RFZ \quad (S9)$$

$$MW = MW - RFZ \quad (S10)$$

921 The remaining meltwater (MW) that exceeds the snowpack's holding capacity (cwh) contributes

← Formatted: Header

← Formatted: Font color: Auto

← Formatted Table

← Formatted Table

← Formatted Table

← Formatted Table

← Formatted: Header

922 to soil infiltration (IF), and the rest remains in the meltwater (MW) storage as

$$IF = \begin{cases} MW - cwh * SNP & MW - cwh * SNP \geq 0 \\ 0 & MW - cwh * SNP < 0 \end{cases} \quad (S11)$$

$$MW = MW - IF \quad (S12)$$

← Formatted Table

923 The fraction of soil moisture relative to the field capacity (fc) determines the soil wetness,
924 which modulates the amount of water recharged into the soil (SP). Then soil moisture (SM) is
925 updated based on the infiltration of meltwater (IF), rain (RN), and the amount of recharged
926 water (SP) as

$$SP = \left(\frac{SM}{fc} \right)^\beta \cdot (IF + RN) \quad (S13)$$

$$SM = SM + IF + RN - SP \quad (S14)$$

← Formatted Table

927 The excess water, above the field capacity (IF_{dir}), is calculated and subsequently removed from
928 the soil moisture storage as

$$IF_{dir} = \begin{cases} SM - fc & if SM \geq fc \\ 0 & if SM < fc \end{cases} \quad (S15)$$

$$SM = SM - IF_{dir} \quad (S16)$$

← Formatted Table

929 Actual evapotranspiration (AE) is determined by an evaporation factor (PEC), which depends
930 on the soil moisture, a shape parameter (λ), a parameter (lp), and field capacity (fc) for
931 evapotranspiration. This factor limits the actual evapotranspiration (AE) to both the potential
932 evapotranspiration (PE) and the available soil moisture.

$$PEC = \begin{cases} \left(\frac{SM}{lp \cdot fc} \right)^\lambda & if 0 \leq \left(\frac{SM}{lp \cdot fc} \right)^\lambda < 1 \\ 0 & if S \left(\frac{SM}{lp \cdot fc} \right)^\lambda < 0 \\ 1 & if S \left(\frac{SM}{lp \cdot fc} \right)^\lambda \geq 1 \end{cases} \quad (S17)$$

$$AE = \begin{cases} PE \cdot PEC & if SM \geq PE \cdot PEC \\ SM & if SM < PE \cdot PEC \end{cases} \quad (S18)$$

$$SM = SM - AE \quad (S19)$$

← Formatted Table

933 Capillary rise (CP) from the lower soil zone (SLZ) is governed by a parameter (c), which
934 determines the amount of water moving upward based on the soil moisture content. This
935 capillary flow replenishes the soil moisture, while groundwater interactions occur through
936 recharge processes in the upper (SUZ) and lower (SLZ) groundwater zones.

$$CP = \begin{cases} SLZ & \text{if } SLZ < c \cdot SLZ \cdot \left(1 - \frac{SM}{fc}\right) \\ c \cdot SLZ \cdot \left(1 - \frac{SM}{fc}\right) & \text{if } SLZ \geq c \cdot SLZ \cdot \left(1 - \frac{SM}{fc}\right) \end{cases} \quad (S20)$$

$$SM = SM + CP \quad (S21)$$

$$SLZ = \begin{cases} SLZ - CP & \text{if } SLZ \geq CP \\ 0 & \text{if } SLZ < CP \end{cases} \quad (S22)$$

937 Excess recharge (SP and IF_{dir}) from the soil enters the upper zone, where it either percolates
 938 to the lower zone ($PERC$) based on a constant rate (prc) or contributes to direct runoff (Q_0)
 939 when it exceeds the upper zone threshold (uzl). The generated flow is modeled using
 940 parameters (k_0, k_1, k_2) governing flow from the upper and lower zones. Each of these flows
 941 contributes to runoff (Q_0, Q_1, Q_2), and their respective contributions to streamflow (Q_t) are
 942 modeled over time.

$$SUZ = SUZ + SP + IF_{dir} \quad (S23)$$

$$PERC = \begin{cases} prc & \text{if } SUZ \geq prc \\ SUZ & \text{if } SUZ < prc \end{cases} \quad (S24)$$

$$SUZ = SUZ - PERC \quad (S25)$$

$$Q_0 = \begin{cases} k_0 \cdot (SUZ - uzl) & \text{if } SUZ \geq uzl \\ 0 & \text{if } SUZ < uzl \end{cases} \quad (S26)$$

$$SUZ = SUZ - Q_0 \quad (S27)$$

$$Q_1 = SUZ \cdot k_1 \quad (S28)$$

$$SUZ = SUZ - Q_1 \quad (S29)$$

$$SLZ = SLZ + PERC \quad (S30)$$

$$Q_2 = SLZ \cdot k_2 \quad (S31)$$

$$SLZ = SLZ - Q_2 \quad (S32)$$

$$Q_t = Q_0 + Q_1 + Q_2 \quad (S33)$$

943
 944 Finally, a routing module (Feng et al., 2022) is used to process Q_t to produce the final
 945 streamflow output (Q_t^*). This module with two parameters ($\theta_\alpha, \theta_\tau$) assumes a gamma function
 946 for the unit hydrograph and convolves the unit hydrograph with the runoff as,
 947

$$Q_t^* = \int_0^{t_{max}} \xi(s; \theta_\alpha, \theta_\tau) \cdot Q(t-s) ds \quad (S34)$$

Formatted: Header

Formatted: Font color: Auto

Formatted Table

Formatted: Font color: Auto

Formatted: Font color: Auto

Formatted: Font color: Auto

Formatted Table

Formatted: Font color: Auto

Formatted: Font color: Auto

Formatted: Font color: Auto

Formatted Table

$$\xi(s: \theta_\alpha, \theta_\tau) = \frac{1}{\Gamma(\theta_\alpha)\theta_\tau^{\theta_\alpha}} t^{\theta_\alpha-1} e^{-\frac{t}{\theta_\tau}} \quad (\text{S35})$$

948

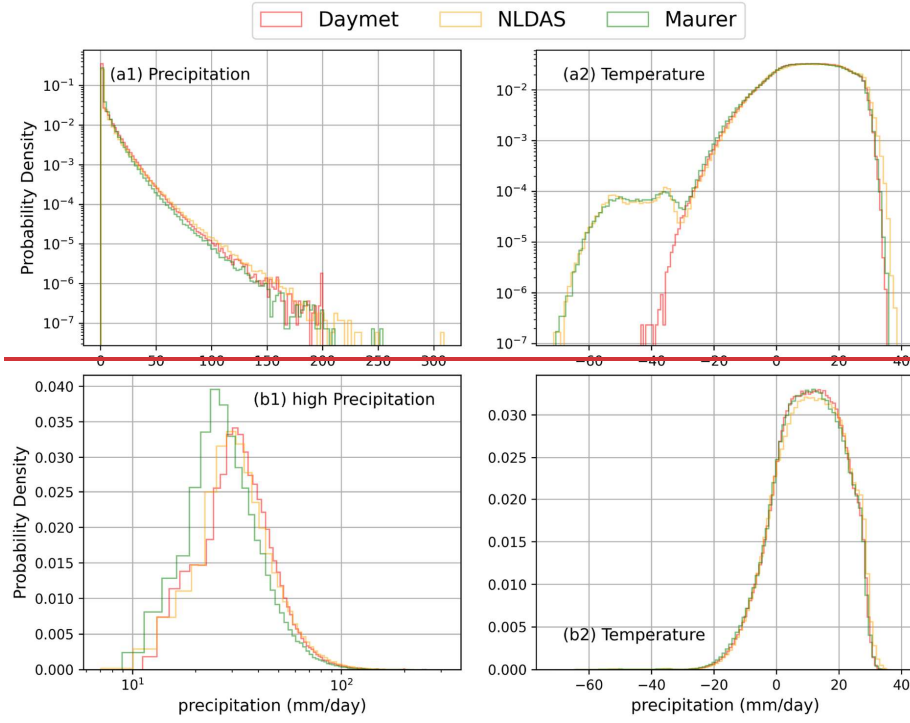
949

950

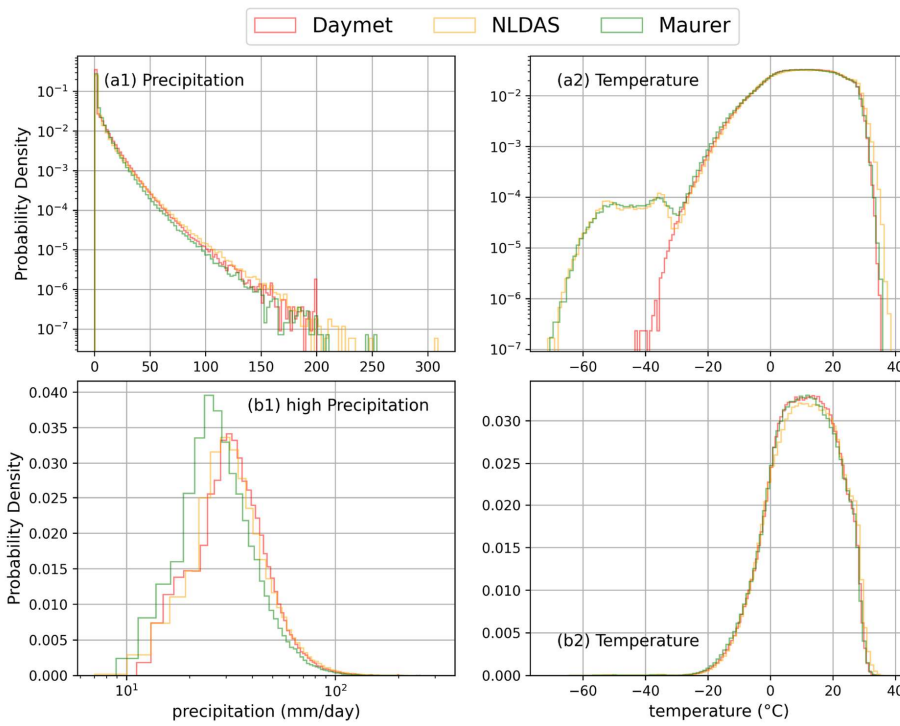
951 **Appendix B: Illustrated differences among the three meteorological forcing datasets**

Formatted: Header

Formatted: Font color: Auto



952

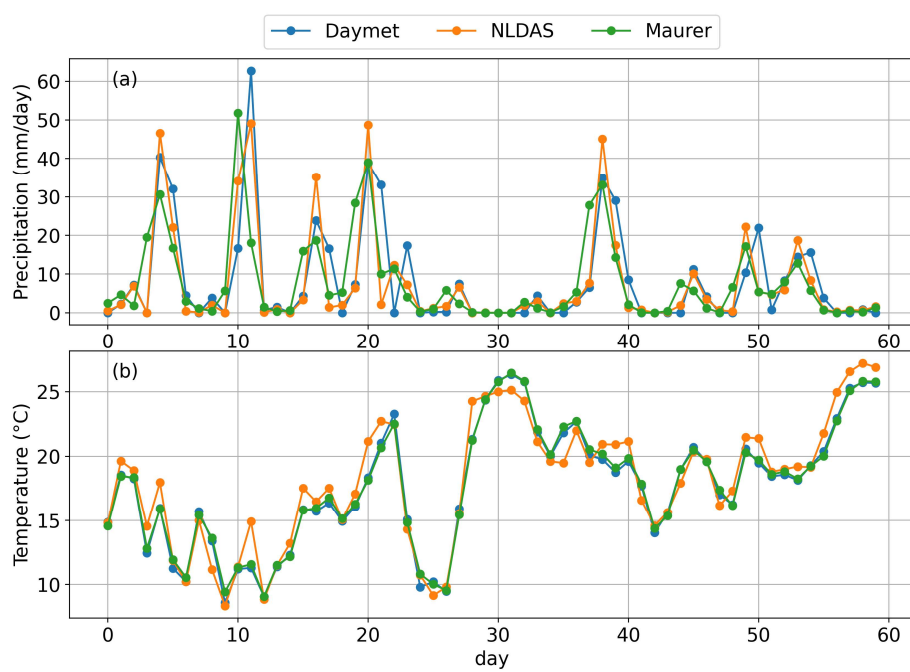
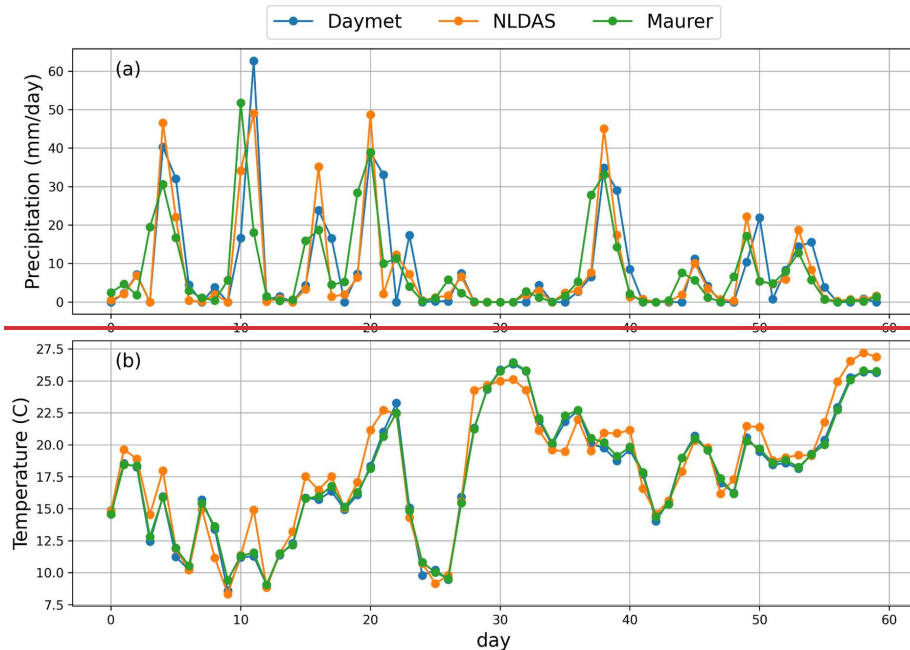


953

954 *Figure B1. Probability density distributions of precipitation and temperature across three*
 955 *meteorological forcing datasets.*

956

957



960 Figure B2. Illustrated temporal variations of precipitation and temperature in a basin across

961 *three meteorological forcing datasets.*
962
963

← Formatted: Header

964 **Appendix C: Details of model inputs, ensemble frameworks, and evaluations**

965 *Table C1. Full names for the abbreviations of dynamic data (all but streamflow are “forcings”)*
 966 *and static basin attributes used as model inputs and outputs. All variables and their values are*
 967 *provided in the CAMELS dataset (Addor et al., 2017) except for the NLDAS and Maurer daily*
 968 *temperature extrema, which are from Kratzert et al. (2021). Potential evapotranspiration and*
 969 *normalized streamflow were calculated for the purposes of in this work, using CAMELS data.*
 970 *The number in parentheses specifies model usage: 1 denotes use in the LSTM model, and 2*
 971 *denotes use in the δHBV model.*

Type	Abbreviation	Full name	Unit
Dynamic data	prcp <u>(1,2)</u>	Precipitation	mm/day
	pet <u>(2)</u>	Potential evapotranspiration (calculated in this work using the Hargreaves equation and CAMELS data)	mm/day
	tmean <u>(2)</u>	Mean air temperature	°C
	tmax <u>(1)</u>	Maximum air temperature	°C
	tmin <u>(1)</u>	Minimum air temperature	°C
	dayl	Day length	s/day
	srad <u>(1)</u>	Shortwave radiation	W/m ²
	vp <u>(1)</u>	Water vapor pressure	pa
	q_vol	Volumetric streamflow	ft ³ /s
	q <u>(1,2)</u>	Streamflow normalized by basin area (q _{vol} / area_gages2)	mm/day
Static basin attributes	p_mean <u>(1,2)</u>	Mean daily precipitation	mm/day
	pet_mean <u>(1,2)</u>	Mean daily potential evapotranspiration	mm/day
	p_seasonality <u>(2)</u>	Seasonality and timing of precipitation	-
	frac_snow <u>(1,2)</u>	Fraction of precipitation falling as snow	-
	aridity <u>(1,2)</u>	Rate of mean values of potential evapotranspiration <u>and</u> precipitation	-
	high_prec_freq <u>(1,2)</u>	Frequency of high precipitation days	days/year
	high_prec_dur <u>(1,2)</u>	Average duration of high precipitation events	days
	low_prec_freq <u>(1,2)</u>	Frequency of dry days	days/year

← Formatted: Header

← Formatted: Font color: Auto

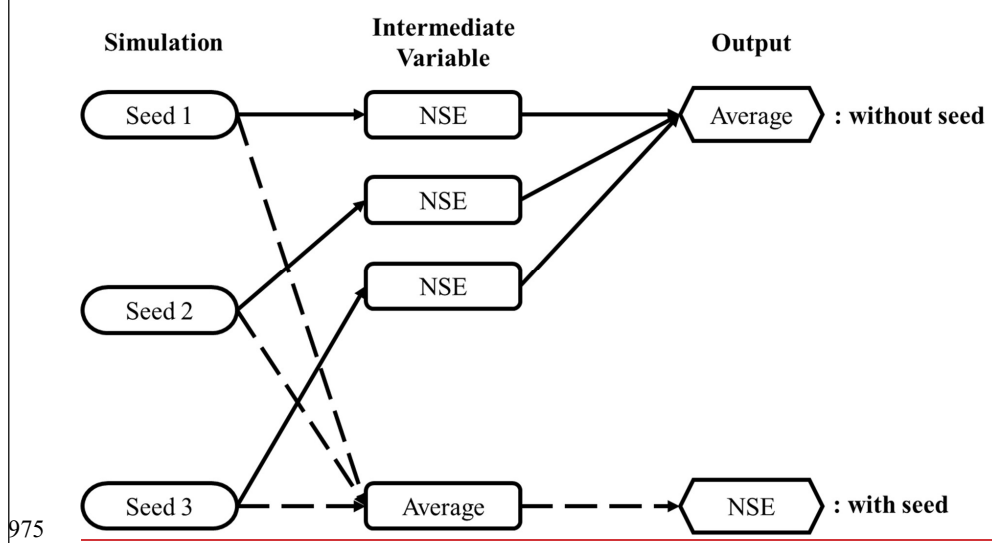
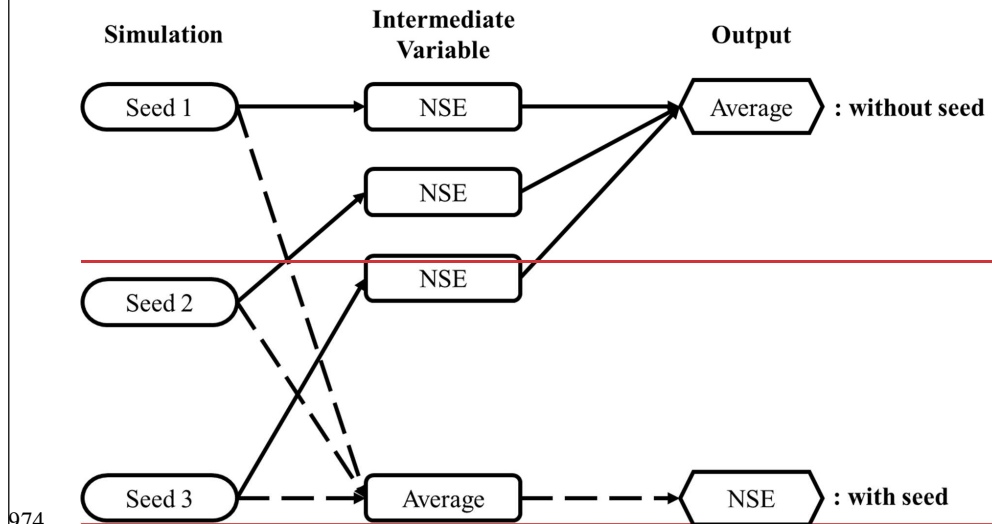
← Formatted Table

low_prec_dur (1,2)	Average duration of dry periods	days
elev_mean (1,2)	Catchment mean elevation	m
slope_mean (1,2)	Catchment mean slope	m/km
area_gages2 (1,2)	Catchment area (GAGES-II estimate)	km ²
frac_forest (1,2)	Fraction of catchment area having land cover identified as forest	-
lai_max (1,2)	Maximum monthly mean of the leaf area index	-
lai_diff (1,2)	Difference between the maximum and minimum monthly mean of the leaf area index	-
gvf_max (1,2)	Maximum monthly mean of the green vegetation	-
gvf_diff (1,2)	Difference between the maximum and minimum monthly mean of the green vegetation fraction	-
dom_land_cover_frac (2)	Fraction of the catchment area associated with the dominant land cover	-
dom_land_cover (2)	Dominant land cover type	-
root_depth_50 (2)	Root depth at 50 th percentile, extracted from a root depth distribution based on the International Geosphere-Biosphere Programme (IGBP) land cover	m
soil_depth_pelletier (1,2)	Depth to bedrock	m
soil_depth_statgso (1,2)	Soil depth	m
soil_porosity (1,2)	Volumetric soil porosity	-
soil_conductivity (1,2)	Saturated hydraulic conductivity	cm/hr
max_water_content (1,2)	Maximum water content	m

sand_frac (1,2)	Fraction of soil which is sand	-
silt_frac (1,2)	Fraction of soil which is silt	-
clay_frac (1,2)	Fraction of soil which is clay	-
geol_class_1st (2)	Most common geologic class in the catchment basin	-
geol_class_1st_frac (2)	Fraction of the catchment area associated with its most common geologic class	-
geol_class_2nd (2)	Second most common geologic class in the catchment basin	-
geol_class_2nd_frac (2)	Fraction of the catchment area associated with its 2nd most common geologic class	-
carbonate_rocks_frac (1,2)	Fraction of the catchment area as carbonate sedimentary rocks	-
geol_porosity (2)	Subsurface porosity	-
geol_permeability (1,2)	Subsurface permeability	m^2

972

973



976 *Figure C1. Ensemble frameworks to generate metrics for ensembles named without (solid
977 arrows) and with (dashed arrows) "seed" as a subscript.*

← Formatted: Header

978 Table C2. Evaluation metrics.

Statistic	Equation*	Range	Optimal Value
NSE	$NSE = 1 - \frac{\sum_{i=1}^n (O_i - S_i)^2}{\sum_{i=1}^n (O_i - \mu_o)^2}$	$-\infty \text{ to } 1.0$	<u>1.0</u>
KGE	$KGE = 1 - \sqrt{(r-1)^2 + (\beta-1)^2 + (\gamma-1)^2},$ $\beta = \frac{\mu_s}{\mu_o}, \gamma = \frac{CV_s}{CV_o} = \frac{\sigma_s/\mu_s}{\sigma_o/\mu_o}$	$-\infty \text{ to } 1.0$	<u>1.0</u>
PBIAS	$\frac{\sum_{i=1}^n (O_i - S_i)}{\sum_{i=1}^n O_i} \times 100$	$-\infty \text{ to } \infty$	<u>0.0</u>
RMSE	$\sqrt{\frac{1}{n} \sum_{i=1}^n (O_i - S_i)^2}$	<u>0.0 to ∞</u>	<u>0.0</u>
spread	$\sqrt{\frac{1}{n} \frac{1}{e} \sum_{i=1}^n \sum_{j=1}^e (S_{i,j} - \mu_{S,i})^2}$	<u>0.0 to ∞</u>	<u>None</u>

Inserted Cells
Inserted Cells

979 * *S* is a streamflow simulation; *O* is the corresponding observation; *n* is the number of total *S*
980 or *O*; *e* is the number of ensemble members; *r* is the linear Pearson correlation between *S* and *O*;
981 *β* is the mean bias; and *γ* is the variability bias. The mean and standard deviation of
982 simulations are denoted as μ_s and σ_s , respectively, and μ_o and σ_o are the mean and standard
983 deviation of the observations.

984

985 *Table C2 (continued). Evaluation metrics.*

Statistic	Range	Optimal Value
NSE	$-\infty$ to 1.0	1.0
KGE	$-\infty$ to 1.0	1.0
PBIAS	$-\infty$ to ∞	0.0
RMSE	0.0 to ∞	0.0

986 * *S* is a streamflow simulation; *O* is the corresponding observation; *n* is the number of total *S*
 987 or *O*; *r* is the linear Pearson correlation between *S* and *O*; β is the mean bias; and γ is the
 988 variability bias. The mean and standard deviation of simulations are denoted as μ_s and σ_s ,
 989 respectively, and μ_o and σ_o are the mean and standard deviation of the observations.

|

990

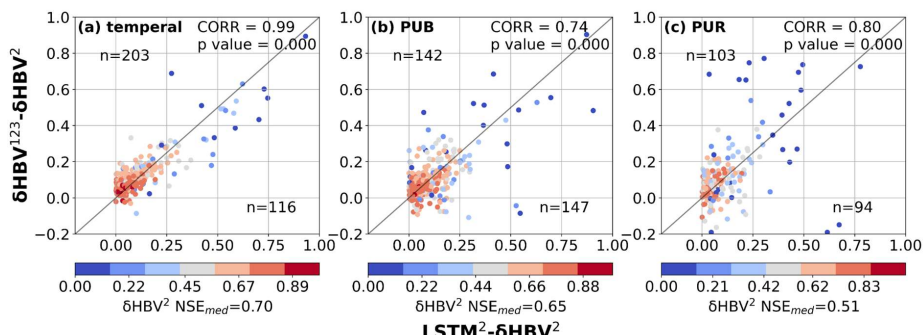
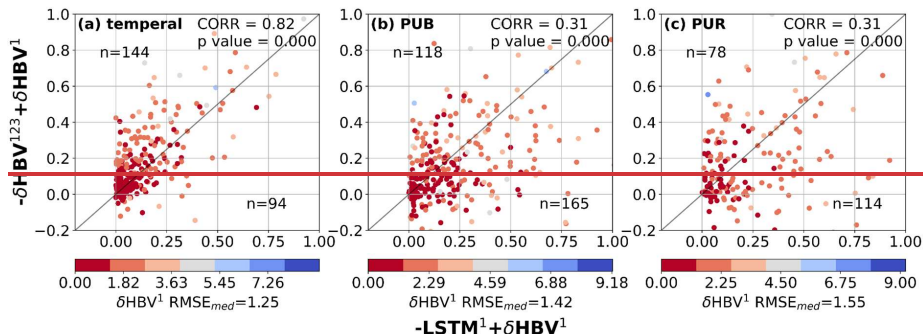
← Formatted: Header

Formatted: Header

Formatted: Font color: Auto

991 Appendix D: Additional details on model performance

992



995 Figure D1. Scatter plots comparing the performance differences between hydrological models:
996 for the basins where LSTM outperformed δHBV (the basins where δHBV outperformed are not
997 shown in this plot). The x-axis represents the RMSE_{NSE} differences between LSTM¹² and
998 δHBV¹δHBV² (LSTM¹² - δHBV¹δHBV²), while the y-axis shows the RMSE_{NSE}
999 differences between δHBV¹²³ and δHBV¹δHBV² (δHBV¹²³ - δHBV¹δHBV²). Points are
1000 color-coded according to the RMSE_{NSE} values of δHBV¹δHBV². The correlation coefficient
1001 (CORR) and p values between the x-axis values and the y-axis values, along with the
1002 median NSE value of δHBV¹ (RMSE_{med} δHBV¹ (NSE_{med})) on these basins, are also noted.
1003

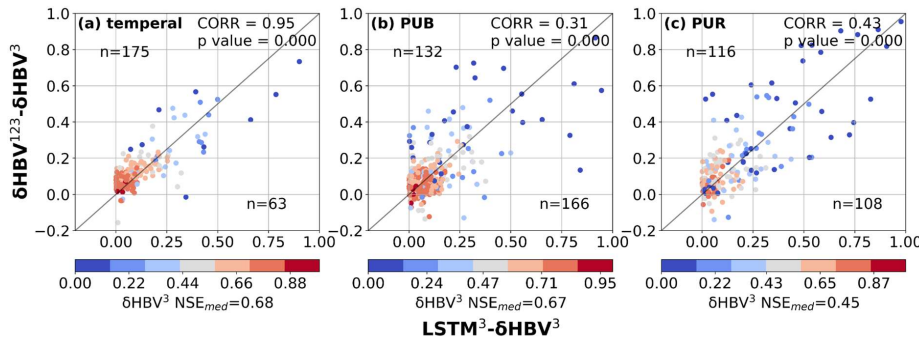


Figure D2. Scatter plots comparing the performance differences between hydrological models for the basins where LSTM outperformed δHBV (the basins where δHBV outperformed are not shown in this plot). The x-axis represents the NSE differences between LSTM^3 and δHBV^3 ($\text{LSTM}^3 - \delta\text{HBV}^3$), while the y-axis shows the NSE differences between δHBV^{123} and δHBV^3 ($\delta\text{HBV}^{123} - \delta\text{HBV}^3$). Points are color-coded according to the NSE values of δHBV^3 . The correlation coefficient (CORR) and p values between the x-axis values and the y-axis values, along with the median NSE value of δHBV^3 (NSE_{med}) on these basins, are also noted.

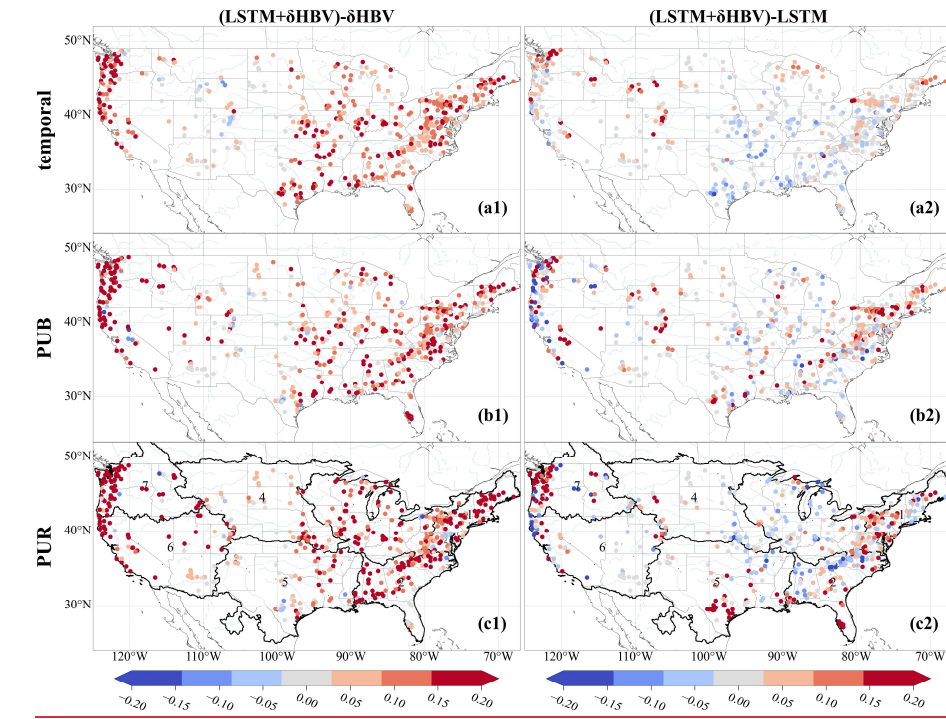
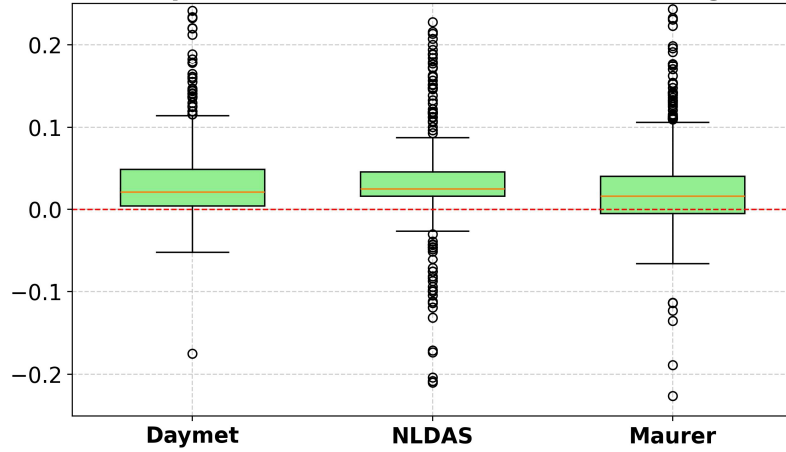


Figure D3. Spatial distributions of model spread values increase from δHBV and LSTM to the LSTM+ δHBV ensemble across temporal, PUB, and PUR tests.

Relative Temperature Differences: (Test – Training) / Training

1022
1023 *Figure D4. Boxplot of relative temperature differences between the test and training periods,*
1024 *calculated as (Test – Training) / Training. Each box represents the distribution of normalized*
1025 *temperature changes across basins for a specific meteorological forcing dataset: Daymet,*
1026 *NLDAS, and Maurer. Positive values indicate warming in the test period relative to the training*
1027 *period.*

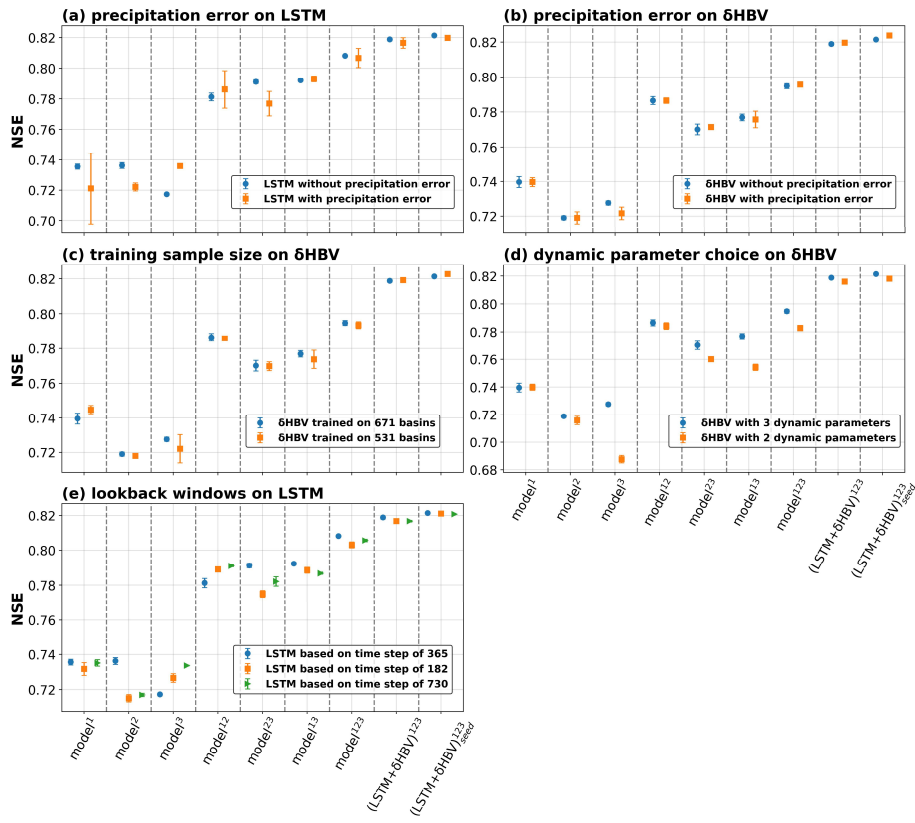


Figure D5. Simulation performance (NSE) under the temporal test: (a) LSTM model with and without a 10% precipitation error (precipitation $\times 1.1$); (b) δHBV model with and without a 10% precipitation error; (c) δHBV model trained on 671 versus 531 basins; (d) δHBV model with 3 versus 2 dynamic parameters; (e) δHBV model using time steps of 365, 182, and 730 days. Individual and ensemble groups are distinguished along the x-axis. Ensemble benefits are indicated by the gap between columns of the same color within each panel—columns 1–7 correspond to individual LSTM or δHBV groups, and the last two columns correspond to LSTM+δHBV ensembles.

1043 Table D1. Median NSE, KGE, RMSE, PBIAS, and RMSE values under low (lowRMSE), high
 1044 (highRMSE), and middle (midRMSE) flows based on 531 basins under the temporal test. The
 1045 values are the mean of three simulations run with different random seeds.

Temporal	Number	Daymet	NLDAS	Maurer
LSTM	NSE	0.735639	0.736301	0.717337
	KGE	0.789375	0.782555	0.760575
	RMSE	1.21088	1.19847	1.27723
	PBIAS	4.04818	5.99486	1.58911
	lowRMSE	0.0596913	0.0602381	0.0545577
	highRMSE	2.70508	2.89684	2.97028
	midRMSE	0.196039	0.210022	0.219922
δHBV	NSE	0.7416417 39688	0.7197767 1903	0.7291427 27669
	KGE	0.7695227 7033	0.7339837 30753	0.7604537 62022
	RMSE	1.1786418 752	1.2686426 239	1.2208923 193
	PBIAS	4.658985. 07898	- 0.2289251 4449	3.1474265 263
	lowRMSE	0.0598199 060906	0.0646098 063581	0.0627206 063466
	highRMSE	2.6918684	3.1519513	2.7162968

← Formatted: Header

← Formatted Table

← Formatted: Header

	<u>79</u>	<u>011</u>	<u>45</u>
midRMSE	0. <u>2287312</u> <u>26595</u>	0. <u>2450142</u> <u>45242</u>	0. <u>2307252</u> <u>30125</u>
LSTM+ δ HBV	NSE	0. <u>7878717</u> <u>87545</u>	0. <u>7931687</u> <u>94053</u>
	KGE	0. <u>7963227</u> <u>94412</u>	0. <u>7836127</u> <u>8383</u>
	RMSE	1. <u>0760407</u> <u>77</u>	1. <u>0674607</u> <u>16</u>
	PBIAS	4. <u>8257259</u> <u>065</u>	3. <u>0815330</u> <u>53</u>
	lowRMSE	0. <u>0599687</u> <u>059955</u>	0. <u>0593688</u> <u>059565</u>
	highRMSE	2. <u>6966570</u> <u>216</u>	2. <u>8224588</u> <u>511</u>
	midRMSE	0. <u>2042612</u> <u>0394</u>	0. <u>2184982</u> <u>14726</u>

1046

1047

1048

1049 Table D1 (continued). Median NSE, KGE, RMSE, PBIAS, and RMSE values under low
 1050 (lowRMSE), high (highRMSE), and middle (midRMSE) flows based on 531 basins under the
 1051 temporal test. The values are the mean of three simulations run with different random seeds.

Temporal	Number	Daymet+NLDAS	Daymet+Maurer	NLDAS+Maurer	A
LSTM	NSE	0.781275	0.791158	0.792144	0.808176
	KGE	0.800955	0.795026	0.794441	0.803476
	RMSE	1.09103	1.06374	1.06701	1.01395
	PBIAS	5.17159	3.34362	4.5305	4.48263
	lowRMSE	0.0636155	0.0582563	0.0566306	0.0613625
	highRMSE	2.70218	2.71366	2.78962	2.67803
	midRMSE	0.194849	0.199809	0.206653	0.197469
δHBV	NSE	0.786118786562	0.77093977012	0.777651776938	0.79445579 4796
	KGE	0.772697773732	0.776781778557	0.767756768854	0.77669277 834
	RMSE	1.0798408362	1.1267112584	1.1087810875	1.05808061 18
	PBIAS	1.8596291507	4.2627828194	4.791342.03584	2.59063710 21
	lowRMSE	0.0627661061667	0.0597778060679	0.0623739062765	0.06178630 61539
	highRMSE	2.9427493961	2.730547394	2.8758388758	2.84511849 94

← Formatted: Header

	midRMSE	0.231984230576	0.219738220743	0.228454230272	0.23013622 8375
LSTM+ δ HBV	NSE	0.8108811825	0.810476809964	0.812144811316	0.81866818 907
	KGE	0.79586797564	0.796202797635	0.78608878735	0.79425779 4936
	RMSE	1.016201938	1.0167601755	1.025150314	1.00077000 67
	PBIAS	4.1307714594	4.0809623333	3.2645819652	3.89728809 6
	lowRMSE	0.0599350603	0.0575384058022	0.0558506057882	0.05818690 59221
	highRMSE	2.7613375275	2.6864267122	2.7824281393	2.71392706 06
	midRMSE	0.208476207637	0.207761205965	0.213433213191	0.20858220 7905

1052

1053 Table D2. Median NSE, KGE, RMSE, PBIAS, and RMSE values under low (lowRMSE), high
 1054 (highRMSE), and middle (midRMSE) flows based on 531 basins under the PUB test. The values
 1055 are the mean of three simulations run with different random seeds.

PUB	Number	Daymet	NLDAS	Maurer
LSTM	NSE	0.702636	0.695496	0.694156
	KGE	0.693998	0.677438	0.6909
	RMSE	1.31714	1.3394	1.34233
	PBIAS	0.669018	0.283106	0.936582
	lowRMSE	0.087648	0.088393	0.086873
	highRMSE	4.2852	4.49292	4.16042
	midRMSE	0.354458	0.364921	0.368124
δHBV	NSE	0.706809	0.670636	0.682998
	KGE	0.703137	0.66566	0.686912
	RMSE	1.35541	1.41185	1.37942
	PBIAS	1.49234	-2.43395	0.291966
	lowRMSE	0.0798196	0.0808967	0.0846775
	highRMSE	4.21648	4.49582	4.18003
	midRMSE	0.335159	0.351271	0.356903
LSTM+δHBV	NSE	0.74227	0.723778	0.72202

← Formatted: Header

← Formatted Table

← Formatted: Header

KGE	0.715931	0.690154	0.707292
RMSE	1.24887	1.278	1.26697
PBIAS	1.27863	-0.599778	0.903464
lowRMSE	0.0816748	0.0795686	0.0825691
highRMSE	4.08432	4.23483	3.94929
midRMSE	0.327459	0.33851	0.347169

1056

1057

1058

← Formatted: Header

1059 Table D2 (continued). Median NSE, KGE, RMSE, PBIAS, and RMSE values under low
1060 (lowRMSE), high (highRMSE), and middle (midRMSE) flows based on 531 basins under the
1061 PUB test. The values are the mean of three simulations run with different random seeds.

PUB	Number	Daymet+NLDAS	Daymet+Maurer	NLDAS+Maurer	← A Formatted Table
LSTM	NSE	0.757853	0.749151	0.753136	0.768181
	KGE	0.713319	0.720099	0.716497	0.727143
	RMSE	1.18251	1.22254	1.19718	1.15026
	PBIAS	0.320396	0.931656	0.766216	0.970047
	lowRMSE	0.0875191	0.0864129	0.0835341	0.0874717
	highRMSE	4.1296	4.06602	4.17217	4.0061
	midRMSE	0.334683	0.349856	0.342819	0.333534
8HBV	NSE	0.748916	0.734052	0.733955	0.757749
	KGE	0.699768	0.714323	0.69436	0.714048
	RMSE	1.26852	1.27637	1.27244	1.23229
	PBIAS	0.0446112	1.212	-1.04135	0.201809
	lowRMSE	0.0808293	0.0792486	0.0814476	0.0808359
	highRMSE	4.19575	3.97788	4.21623	4.07419
	midRMSE	0.311826	0.33668	0.339257	0.318165
LSTM+δHBV	NSE	0.780625	0.764866	0.767761	0.785833

← Formatted: Header

KGE	0.719781	0.725373	0.715982	0.723972
RMSE	1.14924	1.17659	1.16881	1.13591
PBIAS	0.186062	0.881644	0.405548	0.565489
lowRMSE	0.0805946	0.0814251	0.0817114	0.0826379
highRMSE	3.97373	3.86834	3.88	3.91692
midRMSE	0.313708	0.324777	0.324089	0.323671

1062

1063

1064 *Table D3. Median NSE, KGE, RMSE, PBIAS, and RMSE values under low (lowRMSE), high*
 1065 *(highRMSE), and middle (midRMSE) flows based on 531 basins under the PUR test. The values*
 1066 *are the mean of three simulations run with different random seeds.*

PUR	Number	Daymet	NLDAS	Maurer
LSTM	NSE	0.578365	0.546217	0.56164
	KGE	0.557788	0.559986	0.567231
	RMSE	1.59111	1.63626	1.5833
	PBIAS	-0.575328	-2.77709	-0.623183
	lowRMSE	0.124837	0.118971	0.118695
	highRMSE	5.42346	5.38886	5.05212
	midRMSE	0.498133	0.498442	0.471744
8HBV	NSE	0.622278	0.592306	0.59161
	KGE	0.638818	0.601338	0.620877
	RMSE	1.57189	1.61191	1.63628
	PBIAS	1.27223	-1.60075	1.62709
	lowRMSE	0.10142	0.102975	0.101075
	highRMSE	5.07706	5.16093	4.99602
	midRMSE	0.447879	0.474516	0.439697
LSTM+δHBV	NSE	0.644398	0.618255	0.635444

← Formatted: Header

← Formatted Table

← Formatted: Header

KGE	0.627481	0.605237	0.615883
RMSE	1.46185	1.5153	1.48393
PBIAS	-0.269697	-0.719505	0.197859
lowRMSE	0.105146	0.100944	0.106272
highRMSE	4.95749	4.99478	4.78638
midRMSE	0.431456	0.4575	0.426126

1067

1068

1069 Table D3 (continued). Median NSE, KGE, RMSE, PBIAS, and RMSE values under low
 1070 (lowRMSE), high (highRMSE), and middle (midRMSE) flows based on 531 basins under the
 1071 PUR test. The values are the mean of three simulations run with different random seeds.

PUR	Number	Daymet+NLDAS	Daymet+Maurer	NLDAS+Maurer	A
LSTM	NSE	0.634398	0.636369	0.626939	0.656228
	KGE	0.59844	0.600371	0.605007	0.612858
	RMSE	1.4434	1.43416	1.43009	1.38042
	PBIAS	-0.547128	-0.687947	-0.865748	-0.543918
	lowRMSE	0.118989	0.120228	0.115004	0.117728
	highRMSE	5.03277	5.02434	4.84415	4.74281
	midRMSE	0.462923	0.455257	0.453912	0.449598
δHBV	NSE	0.672839	0.644732	0.661231	0.684685
	KGE	0.653841	0.65646	0.6515	0.66205
	RMSE	1.43224	1.50803	1.48604	1.43376
	PBIAS	0.564363	1.55134	-0.156553	0.956961
	lowRMSE	0.0975783	0.0984076	0.100773	0.100807
	highRMSE	4.83843	4.81176	4.72529	4.71255
	midRMSE	0.447828	0.431252	0.433688	0.432018
LSTM+δHBV	NSE	0.685032	0.680872	0.679321	0.700814

← Formatted: Header

KGE	0.638788	0.647826	0.646782	0.649999
RMSE	1.35303	1.3873	1.36795	1.3185
PBIAS	-0.0150729	0.406127	-0.135091	-0.0232668
lowRMSE	0.103284	0.101814	0.104528	0.102916
highRMSE	4.80178	4.72583	4.70024	4.70713
midRMSE	0.426819	0.411727	0.41573	0.41081

1072

1073

1074 Table D4. Median NSE, KGE, RMSE, PBIAS, and RMSE values under low (lowRMSE), high
 1075 (highRMSE), and middle (midRMSE) flows based on 531 basins under the temporal, PUB, and
 1076 PUR tests of $LSTM^{multi}$, $(LSTM + \delta HBV)^{123}$ + $LSTM^{multi}$, their “seed” version, and
 1077 $(LSTM + \delta HBV)_{seed}^{123}$.

Test	Metric	$LSTM^{multi}$	$(LSTM + \delta HBV)^{123}$ + $LSTM^{multi}$
Temporal	NSE	0.797448	0.82321
	KGE	0.811064	0.810248
	RMSE	1.05987	0.983168
	PBIAS	3.95241	4.08594
	lowRMSE	0.056221	0.05702
	highRMSE	2.7089	2.58881
	midRMSE	0.183526	0.192442
PUB	NSE	0.750605	0.782727
	KGE	0.71469	0.734731
	RMSE	1.20586	1.11509
	PBIAS	0.475674	0.706777
	lowRMSE	0.0861127	0.0836
	highRMSE	4.13615	3.83009
	midRMSE	0.347562	0.326814

← Formatted: Header

← Formatted Table

← Formatted: Header

PUR	NSE	0.623755	0.68923
	KGE	0.593757	0.633971
	RMSE	1.47379	1.31221
	PBIAS	-2.6737	-1.38119
	lowRMSE	0.112434	0.107646
	highRMSE	4.98202	4.59232
	midRMSE	0.501807	0.436811

1078

1079 Table D4 (continued). Median NSE, KGE, RMSE, PBIAS, and RMSE values under low
 1080 (lowRMSE), high (highRMSE), and middle (midRMSE) flows based on 531 basins under the
 1081 temporal, PUB, and PUR tests of $LSTM^{multi}$, $(LSTM + \delta HBV)^{123}$ + $LSTM^{multi}$, their “seed”
 1082 version, and $(LSTM + \delta HBV)^{123}_{seed}$.

Test	Metric	$(LSTM + \delta HBV)^{123}_{seed}$	$LSTM^{multi}_{seed}$	$(LSTM + \delta HBV)^{123}_{seed}$ + $LSTM^{multi}_{seed}$
Temporal	NSE	0.821444	0.81992	0.829385
	KGE	0.795317	0.82078	0.812581
	RMSE	0.99455	1.00908	0.967779
	PBIAS	3.99009	4.09469	4.08882
	lowRMSE	0.059782	0.057346	0.057015
	highRMSE	2.7279	2.62815	2.58384
	midRMSE	0.209943	0.183656	0.195557
PUB	NSE	0.793673	0.781175	0.790921
	KGE	0.726188	0.736191	0.739284
	RMSE	1.12957	1.13079	1.09176
	PBIAS	0.370674	1.13671	0.869057
	lowRMSE	0.083423	0.084038	0.085728
	highRMSE	3.89363	3.93473	3.79505
	midRMSE	0.323045	0.329772	0.325627

← Formatted: Header

← Formatted Table

← Formatted: Header

PUR	NSE	0.705154	0.665723	0.701504
	KGE	0.651538	0.614649	0.64373
	RMSE	1.30377	1.3727	1.2851
	PBIAS	-0.283645	-2.74069	-1.39149
	lowRMSE	0.100525	0.111229	0.108121
	highRMSE	4.74889	4.88127	4.58344
	midRMSE	0.406797	0.473783	0.432447

1083

← Formatted: Indent: First line: 0.33"

1084 *Table D5. Median NSE values based on ten different random seeds during the temporal test.*
1085 *Each number (1 through 10) represents metric values calculated for an individual simulation*
1086 *based on only one random seed. “Seed” indicates metric values calculated by averages of these*
1087 *ten simulations based on different random seeds, while “mean” denotes the average of metrics*
1088 *from 1-10 individual simulations (visualized in Figure C1).*

Number	$LSTM^{multi}$	$(LSTM + \delta HBV)^{123}$	$(LSTM + \delta HBV)^{123} + LSTM^{multi}$
1	0.797742	0.818436	0.82315
2	0.795312	0.820188	0.823559
3	0.799291	0.818097	0.822922
4	0.796388	0.818251	0.821791
5	0.791192	0.818285	0.820132
6	0.795691	0.81966	0.823268
7	0.795912	0.821511	0.82352
8	0.796625	0.81831	0.825204
9	0.794062	0.804959	0.816497
10	0.796066	0.817122	0.82169
Seed	0.82425	0.822528	0.832197
Mean	0.795828	0.817482	0.822173

1089

← Formatted: Header

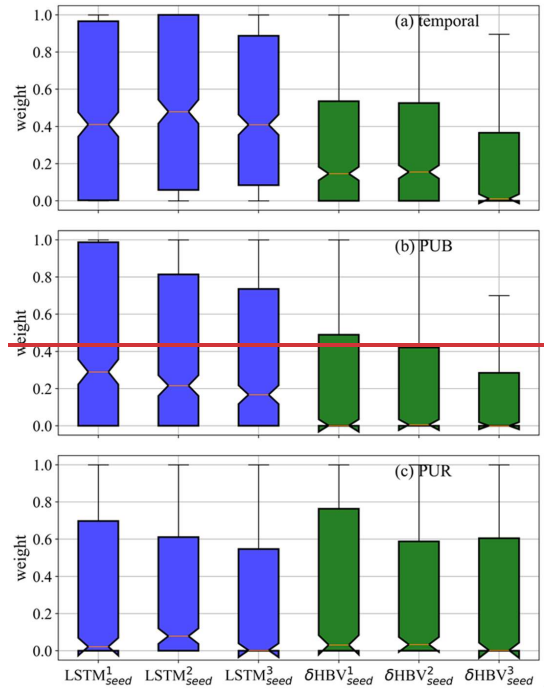
← Formatted Table

← Formatted: Header

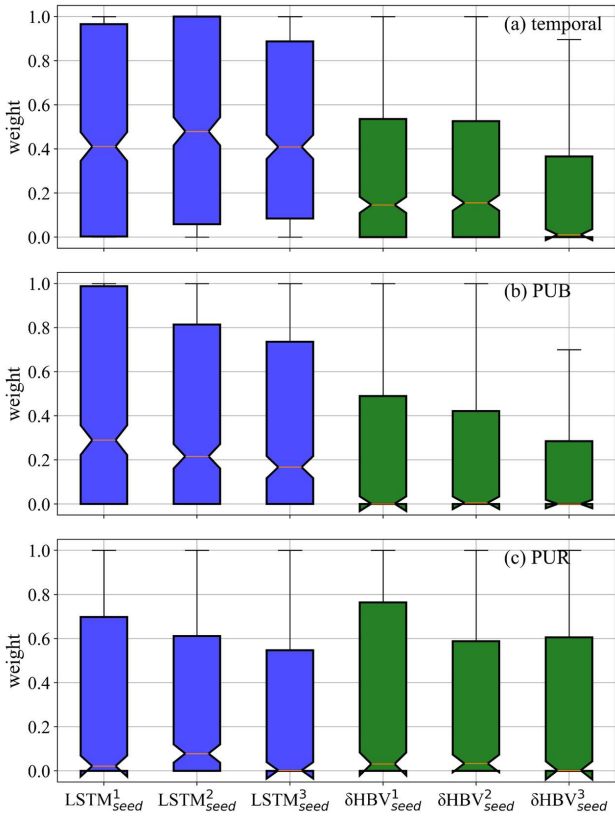
1090 **Appendix E: Intuitive visualization of the relative contributions of ensemble members**

← Formatted: Font color: Auto

1091 based on optimized weights



1092



1093

1094 *Figure E1. Weights of six components across 531 basins, estimated basin-by-basin using a*
 1095 *genetic algorithm based on streamflow observations during the test periods. The weights are*
 1096 *normalized by the maximum weight within each ensemble group. These weights are used*
 1097 *exclusively for qualitatively analyzing the relative contributions of different ensemble members,*
 1098 *with higher values indicating larger relative contributions.*

1099

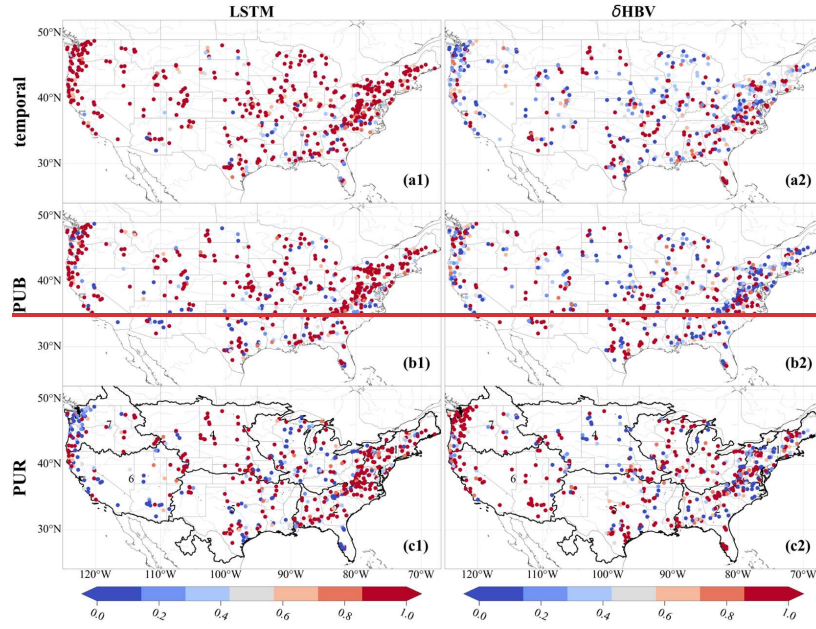
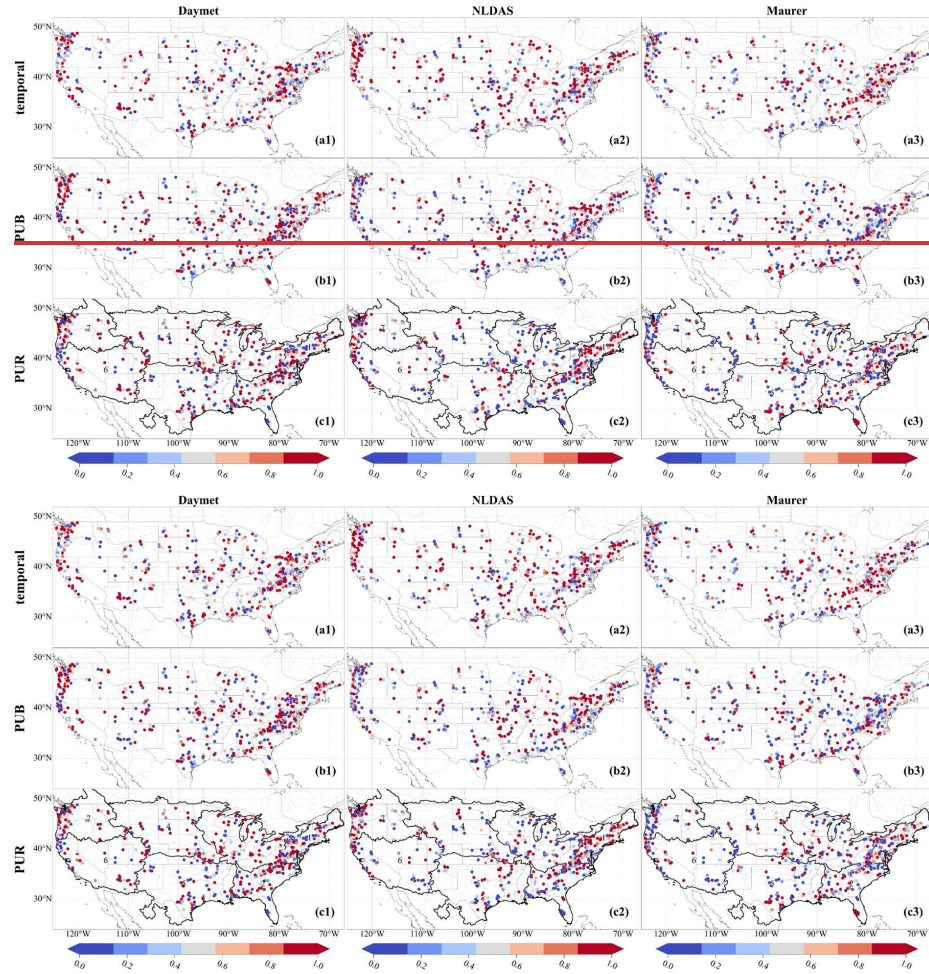


Figure E2. Spatial distributions of weights of the LSTM and δ HBV models, estimated by a

1103 *genetic algorithm based on streamflow observations during the test periods. The weights are*
 1104 *normalized by the maximum weight within each ensemble group. These weights are used*
 1105 *exclusively for qualitatively analyzing the relative contributions of different ensemble members,*
 1106 *with higher values indicating larger relative contributions.*

1107

1108



1109

1110
 1111 *Figure E3. Spatial distributions of weights of the Daymet, NLDAS, and Maurer meteorological*
 1112 *forcing datasets, estimated by a genetic algorithm based on streamflow observations during*
 1113 *the test periods. The weights are normalized by the maximum weight within each ensemble*
 1114 *group. These weights are used exclusively for qualitatively analyzing the relative contributions*

← Formatted: Header

1115 *of different ensemble members, with higher values indicating larger relative contributions.*

1116

1117

1118

1119 *Table E1. Comparisons of metric values between averaged ensemble simulations and*
 1120 *optimized weighted simulations, estimated using a genetic algorithm based on streamflow*
 1121 *observations during the test periods. The results highlight the potential for further*
 1122 *improvements in ensemble simulations.*

1123

	Temporal	Averaged	Optimized weighted
Temporal	NSE	0.8214439128214 44	0.844303212
	KGE	0.7953174957953 17	0.829996445
	RMSE	0.9945500829945 5	0.920954559
	PBIAS	3.9900945919900 9	3.252278013
	lowRMSE	0.0597816160597 82	0.057137161
	highRMSE	2.727901337279	2.451194907
	midRMSE	0.2099426320994 3	0.183127162
PUB	NSE	0.793673	0.842396015
	KGE	0.726188	0.79571295
	RMSE	1.12957	0.987170488
	PBIAS	0.370674	1.023040859
	lowRMSE	0.0834234	0.079807878
	highRMSE	3.89363	3.030715903
PUR	midRMSE	0.323045	0.285110115
	NSE	0.705154	0.790796063
	KGE	0.651538	0.746396324

← Formatted: Header

← Formatted: Justified, Line spacing: single

← Formatted Table

← Formatted: Justified, Line spacing: single

RMSE	1.30377	1.13058149
PBIAS	-0.283645	0.273698787
lowRMSE	0.100525	0.093595304
highRMSE	4.74889	3.665495069
midRMSE	0.406797	0.351694421

← Formatted: Header

← Formatted: Justified, Line spacing: single

1|25
1|26

← Formatted: Header

1127 **Code and data availability**

Formatted: Header

Formatted: Font color: Auto

1128 The source codes and datasets utilized in this study are publicly accessible through the
1129 following repositories: The δHBV modeling framework, including all computational scripts
1130 and documentation, is hosted on Zenodo (<https://doi.org/10.5281/zenodo.7091334>) (Feng et al.,
1131 2023a), with an updated version and comprehensive software release scheduled upon
1132 manuscript acceptance. The implementation of the LSTM architecture is accessible through
1133 Zenodo (<https://doi.org/10.5281/zenodo.6326394>) (Kratzert et al., 2022). The CAMELS
1134 hydrometeorological dataset, which provides the foundational basin characteristics and time
1135 series data used in our analysis, can be obtained via <https://dx.doi.org/10.5065/D6MW2F4D>
1136 (Addor et al., 2017; Newman and Clark, 2014). The streamflow simulations produced in this
1137 study will be made available on Zenodo upon acceptance of the manuscript.

1138

1139 **Author contributions**

Formatted: Font color: Auto

1140 PL and CS designed the experiments and PL carried them out. YS developed the modified
1141 δHBV code. PL prepared the manuscript with contributions from all co-authors.

1142

1143 **Competing interests**

Formatted: Font color: Auto

1144 Chaopeng Shen and Kathryn Lawson have financial interests in HydroSapient, Inc., a
1145 company that could potentially benefit from the results of this research. This interest has been
1146 reviewed by the Pennsylvania State University in accordance with its individual conflict of
1147 interest policy for the purpose of maintaining the objectivity and the integrity of research. The
1148 other authors have no competing interests to declare.

1149

1150 **Acknowledgments**

Formatted: Font color: Auto

1151 PL, CS, and KL were supported by the Office of Biological and Environmental Research

← Formatted: Header

1152 of the U.S. Department of Energy (contract no. DESC0016605). PJ and MP were also partially
1153 supported by California Department of Water Resources Atmospheric River Program Phase III
1154 (Grant 4600014294). YS and CS were partially supported by subaward A23-0252-S002 from
1155 the Cooperative Institute for Research to Operations in Hydrology (CIROH) through the
1156 National Oceanic and Atmospheric Administration (NOAA) Cooperative Agreement (Grant
1157 no. NA22NWS4320003).

1158

1159 References

← Formatted: Font color: Auto

1160 Aboelyazeed, D., Xu, C., Hoffman, F. M., Liu, J., Jones, A. W., Rackauckas, C., Lawson, K.,
1161 and Shen, C.: A differentiable, physics-informed ecosystem modeling and learning framework
1162 for large-scale inverse problems: demonstration with photosynthesis simulations,
1163 Biogeosciences, 20, 2671–2692, <https://doi.org/10.5194/bg-20-2671-2023>, 2023.

1164 Addor, N., Newman, A. J., Mizukami, N., and Clark, M. P.: The CAMELS data set: catchment
1165 attributes and meteorology for large-sample studies, Hydrol. Earth Syst. Sci., 21, 5293–5313,
1166 <https://doi.org/10.5194/hess-21-5293-2017>, 2017.

1167 Aghakouchak, A. and Habib, E.: Application of a Conceptual Hydrologic Model in Teaching
1168 Hydrologic Processes, International Journal of Engineering Education, 26, 2010.

1169 Bandai, T. and Ghezzehei, T. A.: Physics-informed neural networks with monotonicity
1170 constraints for Richardson-Richards equation: Estimation of constitutive relationships and soil
1171 water flux density from volumetric water content measurements, Water Resources Research,
1172 57, e2020WR027642, <https://doi.org/10.1029/2020wr027642>, 2021.

1173 Beck, H. E., van Dijk, A. I. J. M., de Roo, A., Dutra, E., Fink, G., Orth, R., and Schellekens,
1174 J.: Global evaluation of runoff from 10 state-of-the-art hydrological models, Hydrology and
1175 Earth System Sciences, 21, 2881–2903, <https://doi.org/10.5194/hess-21-2881-2017>, 2017.

1176 Beck, H. E., Pan, M., Lin, P., Seibert, J., Dijk, A. I. J. M. van, and Wood, E. F.: Global fully
1177 distributed parameter regionalization based on observed streamflow from 4,229 headwater
1178 catchments, Journal of Geophysical Research: Atmospheres, 125, e2019JD031485,
1179 <https://doi.org/10.1029/2019JD031485>, 2020.

1180 Behnke, R., Vavrus, S., Allstadt, A., Albright, T., Thogmartin, W. E., and Radeloff, V. C.:
1181 Evaluation of downscaled, gridded climate data for the conterminous United States, Ecological
1182 Applications, 26, 1338–1351, <https://doi.org/10.1002/15-1061>, 2016.

1183 Bell, V. A. and Moore, R. J.: The sensitivity of catchment runoff models to rainfall data at
1184 different spatial scales, Hydrology and Earth System Sciences, 4, 653–667,
1185 <https://doi.org/10.5194/hess-4-653-2000>, 2000.

1186 Bergström, S.: Development and application of a conceptual runoff model for Scandinavian

1187 catchments, PhD Thesis, Swedish Meteorological and Hydrological Institute (SMHI),
1188 Norköping, Sweden, 1976.

1189 Bergström, S.: The HBV model—its structure and applications, SMHI, 1992.

1190 Bindas, T., Tsai, W.-P., Liu, J., Rahmani, F., Feng, D., Bian, Y., Lawson, K., and Shen, C.:
1191 Improving river routing using a differentiable Muskingum-Cunge model and physics-informed
1192 machine learning, Water Resources Research, 60, e2023WR035337,
1193 <https://doi.org/10.1029/2023WR035337>, 2024.

1194 Bodnar, C., Bruinsma, W. P., Lucic, A., Stanley, M., Allen, A., Brandstetter, J., Garvan, P.,
1195 Riechert, M., Weyn, J. A., Dong, H., Gupta, J. K., Thambiratnam, K., Archibald, A. T., Wu,
1196 C.-C., Heider, E., Welling, M., Turner, R. E., and Perdikaris, P.: A foundation model for the
1197 Earth system, Nature, 641, 1180–1187, <https://doi.org/10.1038/s41586-025-09005-y>, 2025.

1198 Brunner, M. I., Slater, L., Tallaksen, L. M., and Clark, M.: Challenges in modeling and
1199 predicting floods and droughts: A review, WIREs Water, 8, e1520,
1200 <https://doi.org/10.1002/wat2.1520>, 2021.

1201 Clark, M. P., Slater, A. G., Rupp, D. E., Woods, R. A., Vrugt, J. A., Gupta, H. V., Wagener,
1202 T., and Hay, L. E.: Framework for Understanding Structural Errors (FUSE): A modular
1203 framework to diagnose differences between hydrological models, Water Resources Research,
1204 44, <https://doi.org/10/chvc6k>, 2008.

1205 Clark, M. P., Nijssen, B., Lundquist, J. D., Kavetski, D., Rupp, D. E., Woods, R. A., Freer, J.
1206 E., Gutmann, E. D., Wood, A. W., Brekke, L. D., Arnold, J. R., Gochis, D. J., and Rasmussen,
1207 R. M.: A unified approach for process-based hydrologic modeling: 1. Modeling concept, Water
1208 Resources Research, 51, 2498–2514, <https://doi.org/10/f7db99>, 2015.

1209 Clark, M. P., Wilby, R. L., Gutmann, E. D., Vano, J. A., Gangopadhyay, S., Wood, A. W.,
1210 Fowler, H. J., Prudhomme, C., Arnold, J. R., and Brekke, L. D.: Characterizing uncertainty of
1211 the hydrologic impacts of climate change, Curr Clim Change Rep, 2, 55–64,
1212 <https://doi.org/10.1007/s40641-016-0034-x>, 2016.

1213 Dion, P., Martel, J.-L., and Arsenault, R.: Hydrological ensemble forecasting using a multi-
1214 model framework, Journal of Hydrology, 600, 126537,
1215 <https://doi.org/10.1016/j.jhydrol.2021.126537>, 2021.

1216 Feng, D., Fang, K., and Shen, C.: Enhancing streamflow forecast and extracting insights using
1217 long-short term memory networks with data integration at continental scales, Water Resources
1218 Research, 56, e2019WR026793, <https://doi.org/10.1029/2019WR026793>, 2020.

1219 Feng, D., Lawson, K., and Shen, C.: Mitigating prediction error of deep learning streamflow
1220 models in large data-sparse regions with ensemble modeling and soft data, Geophysical
1221 Research Letters, 48, e2021GL092999, <https://doi.org/10.1029/2021GL092999>, 2021.

1222 Feng, D., Liu, J., Lawson, K., and Shen, C.: Differentiable, learnable, regionalized process-
1223 based models with multiphysical outputs can approach state-of-the-art hydrologic prediction
1224 accuracy, Water Resources Research, 58, e2022WR032404,
1225 <https://doi.org/10.1029/2022WR032404>, 2022.

1226 Feng, D., Shen, C., Liu, J., Lawson, K., and Beck, H.: differentiable parameter learning (dPL)

1227 + HBV hydrologic model, , <https://doi.org/10.5281/zenodo.7943626>, 2023a.

1228 Feng, D., Beck, H., Lawson, K., and Shen, C.: The suitability of differentiable, physics-
1229 informed machine learning hydrologic models for ungauged regions and climate change impact
1230 assessment, *Hydrology and Earth System Sciences*, 27, 2357–2373,
1231 <https://doi.org/10.5194/hess-27-2357-2023>, 2023b.

1232 Frame, J. M., Kratzert, F., Klotz, D., Gauch, M., Shalev, G., Gilon, O., Qualls, L. M., Gupta,
1233 H. V., and Nearing, G. S.: Deep learning rainfall-runoff predictions of extreme events,
1234 *Hydrology and Earth System Sciences*, 26, 3377–3392, <https://doi.org/10.5194/hess-26-3377-2022>, 2022.

1235 Hanazaki, R., Yamazaki, D., and Yoshimura, K.: Development of a reservoir flood control
1236 scheme for global flood models, *JAMES*, 14, e2021MS002944,
1237 <https://doi.org/10.1029/2021MS002944>, 2022.

1238 Hargreaves, G. H.: Defining and using reference evapotranspiration, *Journal of Irrigation and
1239 Drainage Engineering*, 120, 1132–1139, [https://doi.org/10.1061/\(ASCE\)0733-9437\(1994\)120:6\(1132\)](https://doi.org/10.1061/(ASCE)0733-9437(1994)120:6(1132)), 1994.

1240 He, Y., Chen, M., Wen, Y., Duan, Q., Yue, S., Zhang, J., Li, W., Sun, R., Zhang, Z., Tao, R.,
1241 Tang, W., and Lü, G.: An open online simulation strategy for hydrological ensemble
1242 forecasting, *Environmental Modelling & Software*, 174, 105975,
1243 <https://doi.org/10.1016/j.envsoft.2024.105975>, 2024.

1244 Heidari, H., Arabi, M., Warziniack, T., and Kao, S.-C.: Assessing shifts in regional
1245 hydroclimatic conditions of U.S. river basins in response to climate change over the 21st
1246 century, *Earth's Future*, 8, e2020EF001657, <https://doi.org/10.1029/2020EF001657>, 2020.

1247 Hochreiter, S. and Schmidhuber, J.: Long Short-Term Memory, *Neural Computation*, 9, 1735–
1248 1780, <https://doi.org/10.1162/neco.1997.9.8.1735>, 1997.

1249 Jiang, S., Zheng, Y., and Solomatine, D.: Improving AI system awareness of geoscience
1250 knowledge: Symbiotic integration of physical approaches and deep learning, *Geophys. Res.
1251 Lett.*, 47, e2020GL088229, <https://doi.org/10.1029/2020GL088229>, 2020.

1252 Kling, H., Fuchs, M., and Paulin, M.: Runoff conditions in the upper Danube basin under an
1253 ensemble of climate change scenarios, *Journal of Hydrology*, 424–425, 264–277,
1254 <https://doi.org/10.1016/j.jhydrol.2012.01.011>, 2012.

1255 Kraft, B., Jung, M., Körner, M., Koirala, S., and Reichstein, M.: Towards hybrid modeling of
1256 the global hydrological cycle, *Hydrology and Earth System Sciences*, 26, 1579–1614,
1257 <https://doi.org/10.5194/hess-26-1579-2022>, 2022.

1258 Kratzert, F., Klotz, D., Brenner, C., Schulz, K., and Herrnegger, M.: Rainfall-Runoff modelling
1259 using Long-Short-Term-Memory (LSTM) networks, *Hydrology and Earth System Sciences*,
1260 22, 6005–6022, <https://doi.org/10.17605/OSF.IO/QV5JZ>, 2018.

1261 Kratzert, F., Klotz, D., Herrnegger, M., Sampson, A. K., Hochreiter, S., and Nearing, G. S.:
1262 Toward improved predictions in ungauged basins: Exploiting the power of machine learning,
1263 *Water Resources Research*, 55, 11344–11354, <https://doi.org/10.1029/2019WR025488>, 2019.

1266 Kratzert, F., Klotz, D., Hochreiter, S., and Nearing, G. S.: A note on leveraging synergy in
1267 multiple meteorological data sets with deep learning for rainfall-runoff modeling, *Hydrology*
1268 and *Earth System Sciences*, 25, 2685–2703, <https://doi.org/10.5194/hess-25-2685-2021>, 2021.

1269 Kratzert, F., Gauch, M., Nearing, G., and Klotz, D.: NeuralHydrology — A Python library for
1270 Deep Learning research in hydrology, , <https://doi.org/10.5281/zenodo.6326394>, 2022.

1271 Leube, P. C., de Barros, F. P. J., Nowak, W., and Rajagopal, R.: Towards optimal allocation of
1272 computer resources: Trade-offs between uncertainty quantification, discretization and model
1273 reduction, *Environmental Modelling & Software*, 50, 97–107,
1274 <https://doi.org/10.1016/j.envsoft.2013.08.008>, 2013.

1275 Li, P., Zha, Y., Shi, L., Tso, C. H. M., Zhang, Y., and Zeng, W.: Comparison of the use of a
1276 physical-based model with data assimilation and machine learning methods for simulating soil
1277 water dynamics, *Journal of Hydrology*, 584, 124692,
1278 <https://doi.org/10.1016/j.jhydrol.2020.124692>, 2020a.

1279 Li, P., Zha, Y., Tso, C. H. M., Shi, L., Yu, D., Zhang, Y., and Zeng, W.: Data assimilation of
1280 uncalibrated soil moisture measurements from frequency-domain reflectometry, *Geoderma*,
1281 374, 114432, <https://doi.org/10.1016/j.geoderma.2020.114432>, 2020b.

1282 Li, P., Zha, Y., Shi, L., and Zhong, H.: Identification of the terrestrial water storage change
1283 features in the North China Plain via independent component analysis, *Journal of Hydrology: Regional Studies*, 38, 100955, <https://doi.org/10.1016/j.ejrh.2021.100955>, 2021.

1285 Li, P., Zha, Y., Zuo, B., and Zhang, Y.: A family of soil water retention models based on
1286 sigmoid functions, *Water Resources Research*, 59, e2022WR033160,
1287 <https://doi.org/10.1029/2022WR033160>, 2023a.

1288 Li, P., Zha, Y., and Tso, C.-H. M.: Reconstructing GRACE-derived terrestrial water storage
1289 anomalies with in-situ groundwater level measurements and meteorological forcing data,
1290 *Journal of Hydrology: Regional Studies*, 50, 101528,
1291 <https://doi.org/10.1016/j.ejrh.2023.101528>, 2023b.

1292 Li, P., Zha, Y., Zhang, Y., Michael Tso, C.-H., Attinger, S., Samaniego, L., and Peng, J.: Deep
1293 learning integrating scale conversion and pedo-transfer function to avoid potential errors in
1294 cross-scale transfer, *Water Resources Research*, 60, e2023WR035543,
1295 <https://doi.org/10.1029/2023WR035543>, 2024.

1296 Lin, Y., Wang, D., Zhu, J., Sun, W., Shen, C., and Shangguan, W.: Development of objective
1297 function-based ensemble model for streamflow forecasts, *Journal of Hydrology*, 632, 130861,
1298 <https://doi.org/10.1016/j.jhydrol.2024.130861>, 2024.

1299 Lins, H. F. and Slack, J. R.: Streamflow trends in the United States, *Geophysical Research
1300 Letters*, 26, 227–230, <https://doi.org/10.1029/2021GL096847>, 1999.

1301 Liu, J., Rahmani, F., Lawson, K., and Shen, C.: A multiscale deep learning model for soil
1302 moisture integrating satellite and in situ data, *Geophysical Research Letters*, 49,
1303 e2021GL096847, <https://doi.org/10.1029/2021GL096847>, 2022.

1304 Liu, J., Bian, Y., Lawson, K., and Shen, C.: Probing the limit of hydrologic predictability with
1305 the Transformer network, *Journal of Hydrology*, 637, 131389,

1306 <https://doi.org/10.1016/j.jhydrol.2024.131389>, 2024.

1307 Mai, J., Craig, J. R., Tolson, B. A., and Arsenault, R.: The sensitivity of simulated streamflow
1308 to individual hydrologic processes across North America, *Nat Commun.*, 13, 455,
1309 <https://doi.org/10.1038/s41467-022-28010-7>, 2022.

1310 Maurer, E. P., Wood, A. W., Adam, J. C., Lettenmaier, D. P., and Nijssen, B.: A long-term
1311 hydrologically based dataset of land surface fluxes and states for the conterminous United
1312 States, *Journal of Climate*, 15, 3237–3251, [https://doi.org/10.1175/1520-0442\(2002\)015<3237:ALTHBD>2.0.CO;2](https://doi.org/10.1175/1520-0442(2002)015<3237:ALTHBD>2.0.CO;2), 2002.

1314 Moges, E., Demissie, Y., and Li, H.-Y.: Hierarchical mixture of experts and diagnostic
1315 modeling approach to reduce hydrologic model structural uncertainty, *Water Resources
1316 Research*, 52, 2551–2570, <https://doi.org/10.1002/2015WR018266>, 2016.

1317 Nai, C., Liu, X., Tang, Q., Liu, L., Sun, S., and Gaffney, P. P. J.: A novel strategy for automatic
1318 selection of cross-basin data to improve local machine learning-based runoff models, *Water
1319 Resources Research*, 60, e2023WR035051, <https://doi.org/10.1029/2023WR035051>, 2024.

1320 Narkhede, M. V., Bartakke, P. P., and Sutaone, M. S.: A review on weight initialization
1321 strategies for neural networks, *Artificial Intelligence Review*, 55, 291–322,
1322 <https://doi.org/10.1007/s10462-021-10033-z>, 2022.

1323 Nash, J. E. and Sutcliffe, J. V.: River flow forecasting through conceptual models part I — A
1324 discussion of principles, *Journal of Hydrology*, 10, 282–290, [https://doi.org/10.1016/0022-1694\(70\)90255-6](https://doi.org/10.1016/0022-1694(70)90255-6), 1970.

1326 Nearing, G., Cohen, D., Dube, V., Gauch, M., Gilon, O., Harrigan, S., Hassidim, A., Klotz, D.,
1327 Kratzert, F., Metzger, A., Nevo, S., Pappenberger, F., Prudhomme, C., Shalev, G., Shenzis, S.,
1328 Tekalign, T. Y., Weitzner, D., and Matias, Y.: Global prediction of extreme floods in ungauged
1329 watersheds, *Nature*, 627, 559–563, <https://doi.org/10.1038/s41586-024-07145-1>, 2024.

1330 Newman, A. J. and Clark, M.: A large-sample watershed-scale hydrometeorological dataset for
1331 the contiguous USA, <https://doi.org/10.5065/D6MW2F4D>, 2014.

1332 Newman, A. J., Mizukami, N., Clark, M. P., Wood, A. W., Nijssen, B., Nearing, G., Newman,
1333 A. J., Mizukami, N., Clark, M. P., Wood, A. W., Nijssen, B., and Nearing, G.: Benchmarking
1334 of a Physically Based Hydrologic Model, *Journal of Hydrometeorology*, 18, 2215–2225,
1335 <https://doi.org/10/gbwr9s>, 2017.

1336 Newman, A. J., Clark, M. P., Longman, R. J., and Giambelluca, T. W.: Methodological
1337 intercomparisons of station-based gridded meteorological products: Utility, limitations, and
1338 paths forward, <https://doi.org/10.1175/JHM-D-18-0114.1>, 2019.

1339 Ouyang, W., Lawson, K., Feng, D., Ye, L., Zhang, C., and Shen, C.: Continental-scale
1340 streamflow modeling of basins with reservoirs: Towards a coherent deep-learning-based
1341 strategy, *Journal of Hydrology*, 599, 126455, <https://doi.org/10.1016/j.jhydrol.2021.126455>,
1342 2021.

1343 Paul, P. K., Zhang, Y., Ma, N., Mishra, A., Panigrahy, N., and Singh, R.: Selecting hydrological
1344 models for developing countries: Perspective of global, continental, and country scale models
1345 over catchment scale models, *Journal of Hydrology*, 600, 126561,

1346 <https://doi.org/10.1016/j.jhydrol.2021.126561>, 2021.

1347 [Rahmani, F., Appling, A., Feng, D., Lawson, K., and Shen, C.: Identifying structural priors in](https://doi.org/10.1029/2023WR034420)
 1348 [a hybrid differentiable model for stream water temperature modeling, Water Resources](https://doi.org/10.1029/2023WR034420)
 1349 [Research, 59, e2023WR034420, https://doi.org/10.1029/2023WR034420, 2023.](https://doi.org/10.1029/2023WR034420)

1350 [Reichle, R. H. and Koster, R. D.: Assessing the impact of horizontal error correlations in](https://doi.org/10.1175/1525-7541(2003)004<1229:ATIOHE>2.0.CO;2)
 1351 [background fields on soil moisture estimation, Journal of Hydrometeorology, 4, 1229–1242,](https://doi.org/10.1175/1525-7541(2003)004<1229:ATIOHE>2.0.CO;2)
 1352 [https://doi.org/10.1175/1525-7541\(2003\)004<1229:ATIOHE>2.0.CO;2, 2003.](https://doi.org/10.1175/1525-7541(2003)004<1229:ATIOHE>2.0.CO;2)

1353 [Ryan Bellmore, J., Duda, J. J., Craig, L. S., Greene, S. L., Torgersen, C. E., Collins, M. J., and](https://doi.org/10.1002/wat2.1164)
 1354 [Vittum, K.: Status and trends of dam removal research in the United States, WIREs Water, 4,](https://doi.org/10.1002/wat2.1164)
 1355 [e1164, https://doi.org/10.1002/wat2.1164, 2017.](https://doi.org/10.1002/wat2.1164)

1356 [Sawadekar, K., Song, Y., Pan, M., Beck, H., McCrary, R., Ullrich, P., Lawson, K., and Shen,](https://doi.org/10.1016/j.jhydrol.2025.133320)
 1357 [C.: Improving differentiable hydrologic modeling with interpretable forcing fusion, J. Hydrol.,](https://doi.org/10.1016/j.jhydrol.2025.133320)
 1358 [659, 133320, https://doi.org/10.1016/j.jhydrol.2025.133320, 2025.](https://doi.org/10.1016/j.jhydrol.2025.133320)

1359 [Shen, C., Appling, A. P., Gentine, P., Bandai, T., Gupta, H., Tartakovsky, A., Baity-Jesi, M.,](https://doi.org/10.1038/s43017-023-00450-9)
 1360 [Fenicia, F., Kifer, D., Li, L., Liu, X., Ren, W., Zheng, Y., Harman, C. J., Clark, M., Farthing,](https://doi.org/10.1038/s43017-023-00450-9)
 1361 [M., Feng, D., Kumar, P., Aboelyazeed, D., Rahmani, F., Song, Y., Beck, H. E., Bindas, T.,](https://doi.org/10.1038/s43017-023-00450-9)
 1362 [Dwivedi, D., Fang, K., Höge, M., Rackauckas, C., Mohanty, B., Roy, T., Xu, C., and Lawson,](https://doi.org/10.1038/s43017-023-00450-9)
 1363 [K.: Differentiable modelling to unify machine learning and physical models for geosciences,](https://doi.org/10.1038/s43017-023-00450-9)
 1364 [Nat Rev Earth Environ, 4, 552–567, https://doi.org/10.1038/s43017-023-00450-9, 2023.](https://doi.org/10.1038/s43017-023-00450-9)

1365 [Solanki, H., Vegad, U., Kushwaha, A., and Mishra, V.: Improving streamflow prediction using](https://doi.org/10.1029/2024WR038192)
 1366 [multiple hydrological models and machine learning methods, Water Resources Research, 61,](https://doi.org/10.1029/2024WR038192)
 1367 [e2024WR038192, https://doi.org/10.1029/2024WR038192, 2025.](https://doi.org/10.1029/2024WR038192)

1368 [Song, Y., Bindas, T., Shen, C., Ji, H., Knoben, W. J. M., Lonzarich, L., Clark, M. P., Liu, J.,](https://doi.org/10.22541/essoar.172736277.74497104/v1)
 1369 [van Werkhoven, K., Lemont, S., Denno, M., Pan, M., Yang, Y., Rapp, J., Kumar, M., Rahmani,](https://doi.org/10.22541/essoar.172736277.74497104/v1)
 1370 [F., Thébault, C., Sawadekar, K., and Lawson, K.: High-resolution national-scale water](https://doi.org/10.22541/essoar.172736277.74497104/v1)
 1371 [modeling is enhanced by multiscale differentiable physics-informed machine learning,](https://doi.org/10.22541/essoar.172736277.74497104/v1)
 1372 [https://doi.org/10.22541/essoar.172736277.74497104/v1, 26 September 2024a.](https://doi.org/10.22541/essoar.172736277.74497104/v1)

1373 [Song, Y., Knoben, W. J. M., Clark, M. P., Feng, D., Lawson, K., Sawadekar, K., and Shen, C.:](https://doi.org/10.5194/hess-28-3051-2024)
 1374 [When ancient numerical demons meet physics-informed machine learning: adjoint-based](https://doi.org/10.5194/hess-28-3051-2024)
 1375 [gradients for implicit differentiable modeling, Hydrology and Earth System Sciences, 28,](https://doi.org/10.5194/hess-28-3051-2024)
 1376 [3051–3077, https://doi.org/10.5194/hess-28-3051-2024, 2024b.](https://doi.org/10.5194/hess-28-3051-2024)

1377 [Song, Y., Bindas, T., Shen, C., Ji, H., Knoben, W. J. M., Lonzarich, L., Clark, M. P., Liu, J.,](https://doi.org/10.1029/2024WR038928)
 1378 [van Werkhoven, K., Lamont, S., Denno, M., Pan, M., Yang, Y., Rapp, J., Kumar, M., Rahmani,](https://doi.org/10.1029/2024WR038928)
 1379 [F., Thébault, C., Adkins, R., Halgren, J., Patel, T., Patel, A., Sawadekar, K. A., and Lawson,](https://doi.org/10.1029/2024WR038928)
 1380 [K.: High-resolution national-scale water modeling is enhanced by multiscale differentiable](https://doi.org/10.1029/2024WR038928)
 1381 [physics-informed machine learning, Water Resour. Res., 61, e2024WR038928,](https://doi.org/10.1029/2024WR038928)
 1382 [https://doi.org/10.1029/2024WR038928, 2025a.](https://doi.org/10.1029/2024WR038928)

1383 [Song, Y., Sawadekar, K., Frame, J. M., Pan, M., Clark, M., Knoben, W. J. M., Wood, A. W.,](https://doi.org/10.22541/essoar.172304428.82707157/v2)
 1384 [Lawson, K. E., Patel, T., and Shen, C.: Physics-informed, differentiable hydrologic models for](https://doi.org/10.22541/essoar.172304428.82707157/v2)
 1385 [capturing unseen extreme events, https://doi.org/10.22541/essoar.172304428.82707157/v2,](https://doi.org/10.22541/essoar.172304428.82707157/v2)
 1386 [2025b.](https://doi.org/10.22541/essoar.172304428.82707157/v2)

1387 Thornton, P. E., Running, S. W., and White, M. A.: Generating surfaces of daily meteorological
1388 variables over large regions of complex terrain, *Journal of Hydrology*, 190, 214–251,
1389 [https://doi.org/10.1016/S0022-1694\(96\)03128-9](https://doi.org/10.1016/S0022-1694(96)03128-9), 1997.

1390 Tsai, W.-P., Feng, D., Pan, M., Beck, H., Lawson, K., Yang, Y., Liu, J., and Shen, C.: From
1391 calibration to parameter learning: Harnessing the scaling effects of big data in geoscientific
1392 modeling, *Nat Commun*, 12, 5988, <https://doi.org/10.1038/s41467-021-26107-z>, 2021.

1393 Wada, Y., de Graaf, I. E. M., and van Beek, L. P. H.: High-resolution modeling of human and
1394 climate impacts on global water resources, *Journal of Advances in Modeling Earth Systems*, 8,
1395 735–763, <https://doi.org/10.1029/2016MS001162>, 2016.

1396 Wang, N., Zhang, D., Chang, H., and Li, H.: Deep learning of subsurface flow via theory-
1397 guided neural network, *Journal of Hydrology*, 584, 124700,
1398 <https://doi.org/10.1016/j.jhydrol.2020.124700>, 2020.

1399 West, B. D., Maxwell, R. M., and Condon, L. E.: A scalable and modular reservoir
1400 implementation for large-scale integrated hydrologic simulations, *Hydrology and Earth System
1401 Sciences*, 29, 245–259, <https://doi.org/10.5194/hess-29-245-2025>, 2025.

1402 Wilbrand, K., Taormina, R., ten Veldhuis, M.-C., Visser, M., Hrachowitz, M., Nuttal, J., and
1403 Dahm, R.: Predicting streamflow with LSTM networks using global datasets, *Front. Water*, 5,
1404 <https://doi.org/10.3389/frwa.2023.1166124>, 2023.

1405 Xia, Y., Mitchell, K., Ek, M., Sheffield, J., Cosgrove, B., Wood, E., Luo, L., Alonge, C., Wei,
1406 H., Meng, J., Livneh, B., Lettenmaier, D., Koren, V., Duan, Q., Mo, K., Fan, Y., and Mocko,
1407 D.: Continental-scale water and energy flux analysis and validation for the North American
1408 Land Data Assimilation System project phase 2 (NLDAS-2): 1. Intercomparison and
1409 application of model products, *Journal of Geophysical Research: Atmospheres*, 117,
1410 <https://doi.org/10.1029/2011JD016048>, 2012.

1411 Xie, K., Liu, P., Zhang, J., Han, D., Wang, G., and Shen, C.: Physics-guided deep learning for
1412 rainfall-runoff modeling by considering extreme events and monotonic relationships, *Journal
1413 of Hydrology*, 603, 127043, <https://doi.org/10.1016/j.jhydrol.2021.127043>, 2021.

1414 Yao, L., Libera, D. A., Kheimi, M., Sankarasubramanian, A., and Wang, D.: The roles of
1415 climate forcing and its variability on streamflow at daily, monthly, annual, and long-term scales,
1416 *Water Resources Research*, 56, e2020WR027111, <https://doi.org/10.1029/2020WR027111>,
1417 2020.

1418 Yilmaz, K. K., Gupta, H. V., and Wagener, T.: A process-based diagnostic approach to model
1419 evaluation: Application to the NWS distributed hydrologic model, *Water Resources Research*,
1420 44, <https://doi.org/10.1029/2007WR006088>, 2008.

1421 Yu, D., Yang, J., Shi, L., Zhang, Q., Huang, K., Fang, Y., and Zha, Y.: On the uncertainty of
1422 initial condition and initialization approaches in variably saturated flow modeling, *Hydrology
1423 and Earth System Sciences*, 23, 2897–2914, <https://doi.org/10.5194/hess-23-2897-2019>, 2019.

1424 Yu, M., Huang, Q., and Li, Z.: Deep learning for spatiotemporal forecasting in Earth system
1425 science: a review, *International Journal of Digital Earth*, 17, 2391952,
1426 <https://doi.org/10.1080/17538947.2024.2391952>, 2024.

← Formatted: Header

1427 Zhang, Q., Shi, L., Holzman, M., Ye, M., Wang, Y., Carmona, F., and Zha, Y.: A dynamic
1428 data-driven method for dealing with model structural error in soil moisture data assimilation,
1429 Advances in Water Resources, 132, 103407, <https://doi.org/10.1016/j.advwatres.2019.103407>,
1430 2019.

1431 Zounemat-Kermani, M., Batelaan, O., Fadaee, M., and Hinkelmann, R.: Ensemble machine
1432 learning paradigms in hydrology: A review, Journal of Hydrology, 598, 126266,
1433 <https://doi.org/10.1016/j.jhydrol.2021.126266>, 2021.

← Formatted: Indent: First line: 0"